Evidence of near-ambient superconductivity in a N-doped lutetium hydride

https://doi.org/10.1038/s41586-023-05742-0

Received: 26 April 2022

Accepted: 18 January 2023

Published online: 8 March 2023

Check for updates

Nathan Dasenbrock-Gammon[1,4], Elliot Snider[2,4], Raymond McBride[2,4], Hiranya Pasan[1,4], Dylan Durkee[1,4], Nugzari Khalvashi-Sutter[2], Sasanka Munasinghe[2], Sachith E. Dissanayake[2], Keith V. Lawler[3], Ashkan Salamat[3] & Ranga P. Dias[1,2]✉

The absence of electrical resistance exhibited by superconducting materials would have enormous potential for applications if it existed at ambient temperature and pressure conditions. Despite decades of intense research efforts, such a state has yet to be realized[1,2]. At ambient pressures, cuprates are the material class exhibiting superconductivity to the highest critical superconducting transition temperatures (T_c), up to about 133 K (refs. [3–5]). Over the past decade, high-pressure 'chemical precompression'[6,7] of hydrogen-dominant alloys has led the search for high-temperature superconductivity, with demonstrated T_c approaching the freezing point of water in binary hydrides at megabar pressures[8–13]. Ternary hydrogen-rich compounds, such as carbonaceous sulfur hydride, offer an even larger chemical space to potentially improve the properties of superconducting hydrides[14–21]. Here we report evidence of superconductivity on a nitrogen-doped lutetium hydride with a maximum T_c of 294 K at 10 kbar, that is, superconductivity at room temperature and near-ambient pressures. The compound was synthesized under high-pressure high-temperature conditions and then—after full recoverability—its material and superconducting properties were examined along compression pathways. These include temperature-dependent resistance with and without an applied magnetic field, the magnetization (M) versus magnetic field (H) curve, a.c. and d.c. magnetic susceptibility, as well as heat-capacity measurements. X-ray diffraction (XRD), energy-dispersive X-ray (EDX) and theoretical simulations provide some insight into the stoichiometry of the synthesized material. Nevertheless, further experiments and simulations are needed to determine the exact stoichiometry of hydrogen and nitrogen, and their respective atomistic positions, in a greater effort to further understand the superconducting state of the material.

Dense elemental hydrogen has long been predicted to be a very-high-temperature superconductor[22,23], yet the extremely high pressures required have presented challenges in confirming those superconducting phases[24,25]. The superhydride materials offer the promise of retaining the superconducting properties of dense elemental hydrogen but at much lower pressures. The prediction of a 220–235-K superconducting transition temperature (T_c) in CaH_6 at 150 GPa (ref. [26]) and the watershed discovery of a 203-K T_c for H_3S at 155 GPa (ref. [27]) have instigated a materials discovery boon in which, at present, almost all possible binary systems of high-pressure hydride systems have been modelled[28]. The recent observation of an anomalously high T_c in YH_6 showed that high-temperature superconductivity can be achieved with lower hydrogen content and more modest pressures than previously understood[13]. As the main discoveries have all been at greater than megabar pressures, the goal has shifted to further lowering the pressure required, with a focus on the vast sample space of ternary hydride compounds. One direction is a third, light element acting as a dopant in the metal hydrides, which is predicted to have two main beneficial effects[29]. First, there is a predicted increase in T_c as seen in proposed examples such as critical temperatures approaching 500 K in the Li–Mg–H system, although still in the megabar regime[17], and virtual crystal approximation simulations and recent experimental evidence indicating an increase of the transition temperature by at least 25 K from doping the LaH_{10} framework[18,19,30]. Second, the addition of a third element can greatly enhance the stability of a hydrogen-rich lattice, thereby lowering the pressure range over which it is stable. $LaBH_8$ is predicted to be stable down to 20–40 GPa while maintaining its high-temperature superconductivity[20,21], and a metal–boron–carbon clathrate is predicted to retain its superconducting properties at ambient pressures[31]. The presence of stability combined with increasing T_c by introducing the third element opens the possibility of pushing the hydride superconductors to higher values of T_c at sub-megabar pressures.

[1]Department of Physics and Astronomy, University of Rochester, Rochester, NY, USA. [2]Department of Mechanical Engineering, School of Engineering and Applied Sciences, University of Rochester, Rochester, NY, USA. [3]Unearthly Materials Inc., Rochester, NY, USA. [4]These authors contributed equally: Nathan Dasenbrock-Gammon, Elliot Snider, Raymond McBride, Hiranya Pasan, Dylan Durkee. ✉e-mail: rdias@rochester.edu

As there is an overwhelming amount of phase space unexplored by simulation in ternary rare-earth hydrides, rational chemical design is needed at present to identify the next candidate material. The La and Y binary superhydrides are predicted and measured to adopt similar high-pressure stoichiometries and phases with the Y-based ones exhibiting higher T_c at equivalent pressures[8–10,12]. The smaller size of the Y^{3+} cation offers a simple chemical rationale for this behaviour. However, the Sc hydrides with an even smaller ionic radius are predicted to have completely different structures and lower T_c (ref. [32]). Owing to the lanthanoid contraction, the lanthanoids heavier than Dy offer comparable or smaller trivalent ionic radii than Y but with the complication of *f* electrons[33–35]. Although the 4*f* electrons in lanthanoid compounds are often atom-localized and semivalent at ambient conditions, the inherent magnetism of partially occupied 4*f* states[36–38] or migration towards the Fermi level under pressure could be detrimental to the superconducting properties[9,39]. Although synthesis efforts for the high-pressure YbH_x system have produced structures distinct from its La and Y counterparts, probably owing to the transfer of *d* electrons to unoccupied *f* states[40], predictions indicate that hydrides of the two heaviest lanthanoids should be able to achieve $T_c \geq 145$ K by a megabar owing to the strong electron correlation of the 4*f* electrons near the Fermi level[41]. Causes of the high T_c achieved in the sub-megabar regime are believed to be twofold. First, the over half-filled valence 4*f* states suppress the phonon softening and second they provide some enhancement to the electron–phonon coupling relative to the transition metal (Y and La) rare earths. Combining the benefits of light atom doping and the presence of 4*f* electrons in the valance states should increase the stability of a hydrogen-rich rare-earth hydride to lower pressures while potentially enhancing its superconducting properties.

In this paper, we present experimental evidence of superconductivity at 294 K and 10 kbar pressure in a ternary lutetium–nitrogen–hydrogen compound in which the combination of a full 4*f* shell along with the electron donation and chemical pressure of the nitrogen drive the T_c and pressure stability of nitrogen-doped lutetium hydride into the near-ambient regime. The measured superconducting properties are the observation of zero resistance, a.c. magnetic susceptibility and d.c. magnetic susceptibility with zero field and field cooling, magnetization *M*–*H* curve, heat capacity, voltage–current (*V*–*I*) curves and the reduction of T_c under an external magnetic field with an upper critical magnetic field of about 88 tesla based on the Ginzburg–Landau (GL) model at zero temperature (see Extended Data Fig. 15). The composition and structure are explored with elemental analysis, EDX measurements, XRD, Raman spectroscopy and density functional theory (DFT) simulations.

Temperature–pressure relations and visual change

The near-ambient superconducting stability regime of the ternary lutetium–nitrogen–hydrogen system extends from about 3 kbar to about 30 kbar (Fig. 1a) and is accompanied by a marked visual transformation over just a few kbar of pressure (Fig. 1b). The recovered sample is initially in a non-superconducting metallic phase with a lustrous bluish colour, denoted here as phase I. Compression to about 3 kbar drives the progression of the system into phase II, leading to the onset of the superconducting regime, and this transformation is associated with a sudden change in colour from blue to pink. T_c as determined by electrical-resistance, magnetic-susceptibility and heat capacity-measurements increases with pressure from 171 K at around 5 kbar until it peaks at 294 K at around 10 kbar. The 10-kbar turning point in the superconducting dome is followed by a reduction in T_c to approximately 200 K before about 30 kbar. Compression above the highest pressure T_c shown in Fig. 1a drives the sample through another phase transition into phase III. Phase III is a non-superconducting metallic state that is once again distinct in colour, being bright red in appearance. The colour changes are for reflected light only and the sample is completely opaque for transmitted light.

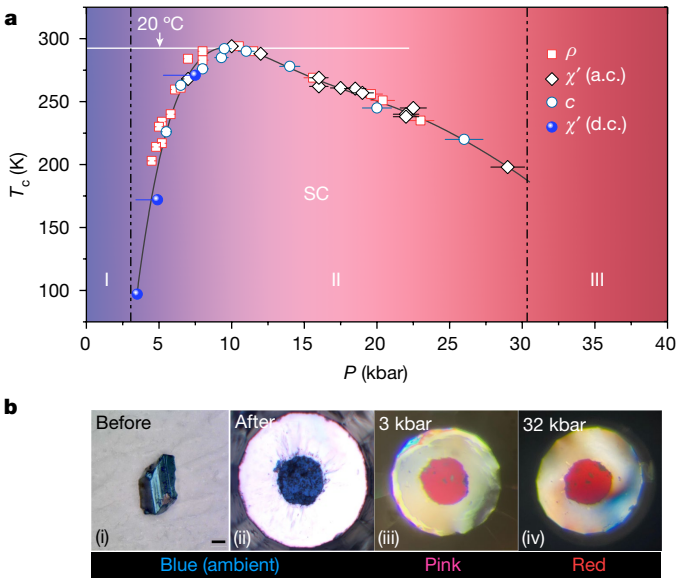

Fig. 1 | Superconductivity in lutetium–nitrogen–hydrogen at near-ambient pressures. a, Evolution of the superconducting transition temperature (T_c) of recompressed nitrogen-doped lutetium hydride as a function of pressure (*P*), illustrating a clear dome-shaped peak around 10 kbar with a T_c of 294 K. Superconductivity (SC) is only observed in phase II between about 3 kbar and about 30 kbar of pressure. *ρ*, electrical resistance; *χ*′ (a.c.), dynamic magnetic susceptibility; *χ*′ (d.c), static magnetic susceptibility; *c*, heat capacity. **b**, Microphotographs of a sample using only reflected light recovered from a metallic sample from high-pressure high-temperature synthesis before being loaded into the diamond anvil cell (i) and after loading at ambient pressure, showing a remarkable blue colour (ii). Scale bar, 10 μm. The sample is completely opaque to transmitted light. Under pressure, the sample transformed from blue to pink at about 3 kbar (iii) and to red at about 30 kbar (iv).

Temperature-dependent electrical resistance

The superconducting transitions of phase II are evidenced by a sharp drop in resistance within a temperature change of a few degrees kelvin (Fig. 2a). The temperature-dependent resistance data were acquired during the natural warming cycle (about 0.25 K min^{-1}) with a current of 100 μA to 2 mA. The accuracy of the temperature probe is ±0.1 K and the transition temperature was determined from the onset of superconductivity. In all experiments, the reported pressure was measured using ruby fluorescence. The transition width in zero applied magnetic field, as observed in other high-T_c hydride systems, has a $\Delta T/T_c$ value ranging from 0.005 to 0.036, and such features are readily explained within the dirty limit as described by GL theory[42]. The *V*–*I* relations are simultaneously measured along with the four-probe electrical-resistance measurements. Figure 2b shows the *V*–*I* characteristics with steadily increasing current measured in zero applied magnetic field. At a temperature above the superconducting transition ($T = 297$ K $> T_c = 294$ K), a linear *V*–*I* response following Ohm's law was observed for the metallic state of nitrogen-doped lutetium hydride at 10 kbar. As the temperature is reduced below T_c ($T = 30$ K) at the same pressure, the voltage drop is immeasurably low (essentially zero) and shows a nonlinear, $V \propto I^{3(2.84)}$ response. The *V*–*I* data were obtained from the *V*, *I* pair, shown in Fig. 2b.

Magnetic susceptibility

Another key criterion for a superconducting material is the demonstration of the Meissner effect. In a type I superconductor, this should—in principle—equate to perfect diamagnetism below the critical field, whereas in a type II superconductor, there exists perfect diamagnetism below the lower critical field and a vortex state between the upper

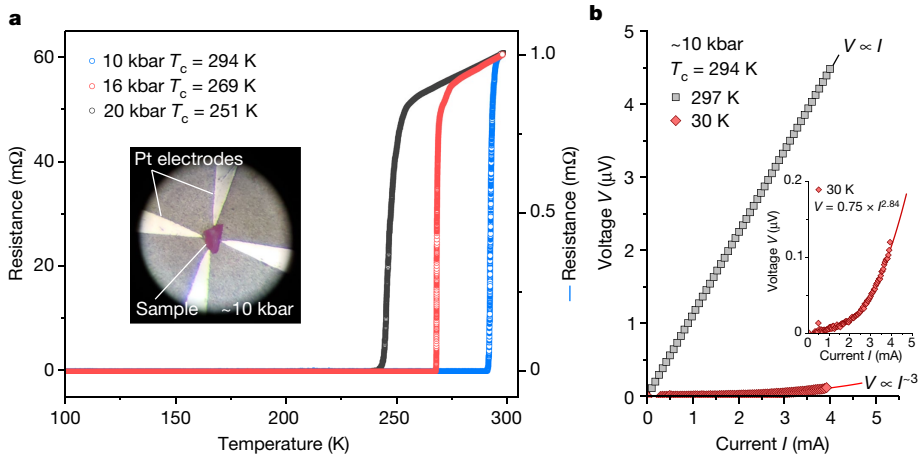

Fig. 2 | Temperature-dependent and field-dependent electrical resistance and *V*–*I* behaviour of the lutetium–nitrogen–hydrogen system. **a**, Temperature-dependent electrical resistance of nitrogen-doped lutetium hydride at high pressures, showing the superconducting transitions as high as 294 K at 10 ± 0.1 kbar, the highest transition temperature measured in all experimental runs. The colours represent the transition at different pressures. The right *y* axis represents the 10-kbar resistance versus temperature in blue colour for a different pair of *V* and *I* contacts. The data were obtained during the warming cycle to minimize the electronic and cooling noise. The inset illustrates the experimental setup for the electrical resistance at around 10 kbar using platinum (Pt) metal probes in a four-probe configuration. **b**, *V*–*I* characteristics measured at temperatures of 297 K and 30 K at 10 kbar. The transition temperature (T_c) is 294 K and above that temperature, the sample exhibits typical linear behaviour. Below T_c (T = 294 K), well within the superconducting regime, at the same pressure, a nonlinear, $V \propto I^{3(2.84)}$ response is shown. The inset highlights the power law *V*–*I* dependence.

and lower critical fields. The temperature dependence of the magnetic moments and *M*–*H* curves at different temperatures were measured on a Quantum Design Physical Property Measurement System (PPMS) by using the Vibrating Sample Magnetometer (VSM) method. Figure 3a shows the d.c. magnetic susceptibility ($\chi = M/H$, in which M is magnetization and H is magnetic field) as a function of temperature, under conditions of zero field cooling (ZFC) and field cooling (FC) at 60 Oe. The existence of the superconducting phase was then confirmed by measuring the Meissner effect on cooling in a magnetic field. The onset of a well-defined Meissner effect was observed at about 277 K at around 8 kbar. The *M*–*H* data were recorded using a PPMS with VSM option (see Fig. 3b). We used an HMD high-pressure cell and Daphne oil as the medium for applying pressure. Compared with a diamond anvil cell (DAC), the maximum pressure achievable is considerably lower in a HMD high-pressure cell. The HMD high-pressure cell is rated to reach a maximum pressure of 13 kbar, although we have not been able to achieve such a pressure. Because the filling factor of the sample is small (limited by the synthesis procedure), achieving the rated 10 kbar will require substantially greater pressure-cell compression. The maximum pressure we were able to generate was about 8 kbar. The pressure dependence of T_c is approximately 30 K kbar^{-1} from about 3 kbar to about 10 kbar. The broad transition is most probably because of the pressure gradient caused by the high-pressure cell and/or by chemical inhomogeneities in the main sample. The temperatures observed for the onset of diamagnetism with ZFC are commensurate with those from the electrical-resistance measurements.

The diamagnetic response of nitrogen-doped lutetium hydride is also seen by a 30–50-nV drop in the real part of temperature-dependent a.c. susceptibility, $\chi'(T)$, for different pressures across the superconducting stability range of phase II (Fig. 3c). The techniques for measuring a.c. susceptibility were similar to those of Snider et al.[14,15] and with respect to background subtraction; here we have used a cubic polynomial (see Extended Data Fig. 5). Given that the trivalent rare-earth elements are extremely reactive, the synthesis can be tricky and, consequently, the amount of superconducting sample can vary and thus the strength of the signal is dependent on volume. On average, sample sizes are on the order of 70–100 μm in diameter and 10–20 μm thick. For larger samples, the strength of the diamagnetic response increases by nearly five times in magnitude (see Extended Data Fig. 6). The transition width (ΔT_c), as observed in other high-T_c hydride systems, has a value of approximately 0.8 K, 2 K and 5 K at T_c of 294 K (at 10 kbar), 269 K (16 kbar) and 238 K (22 kbar), respectively, indicating the pressure broadening. Extended Data Fig. 12 shows the a.c. susceptibility, with the electrical resistance showing similar critical temperatures and very similar transition widths.

a.c. calorimetry of lutetium–nitrogen–hydrogen

The specific heat (C) is an important thermodynamic quantity and is extensively used at ambient pressures to confirm bulk superconductivity. The BCS model superconductors have an energy gap associated with the formation of Cooper pairs, resulting in a spike in the specific heat of a superconductor at T_c. However, detecting such heat anomalies at high pressure is difficult because of the highly thermally conductive environment of the diamonds. In this study, we have used a new setup of the a.c. calorimetric technique for measuring the specific heat[43]. The sample is thermally excited by an a.c. applied at frequency $\omega/2$ to a resistance heater, leading to an a.c. heat power at frequency ω to determine the specific heat capacity (C) of the sample (see Methods for more information). Using the well-known superconducting transition in MgB_2 as a test case (Extended Data Fig. 4), we find that the higher-frequency value on the falling edge of the plateau provides the cleanest response for measurements. A frequency sweep above T_c easily identifies the falling edge of the plateau, and the resultant heat capacity of MgB_2 at 15 kbar shows the distinctive discontinuity of the specific heat capacity at 32 K. Replicating this procedure in the superconducting stability regime of phase II yields specific-heat-capacity curves exhibiting the distinctive discontinuity (Fig. 4a–c). The T_c values identified in this manner are very similar to those found through both electrical resistance and a.c. susceptibility, identifying a bulk nature for the transition and the shape of the superconducting dome shown in Fig. 1a. The highest T_c we have observed using this method is 292 K at about 10 kbar. These measurements are also subject to a sample-size dependency, and the typical samples here are about 60–100 μm in diameter.

Composition and structure

The composition of the superconducting ternary lutetium–nitrogen–hydrogen compound was identified by using a combination of

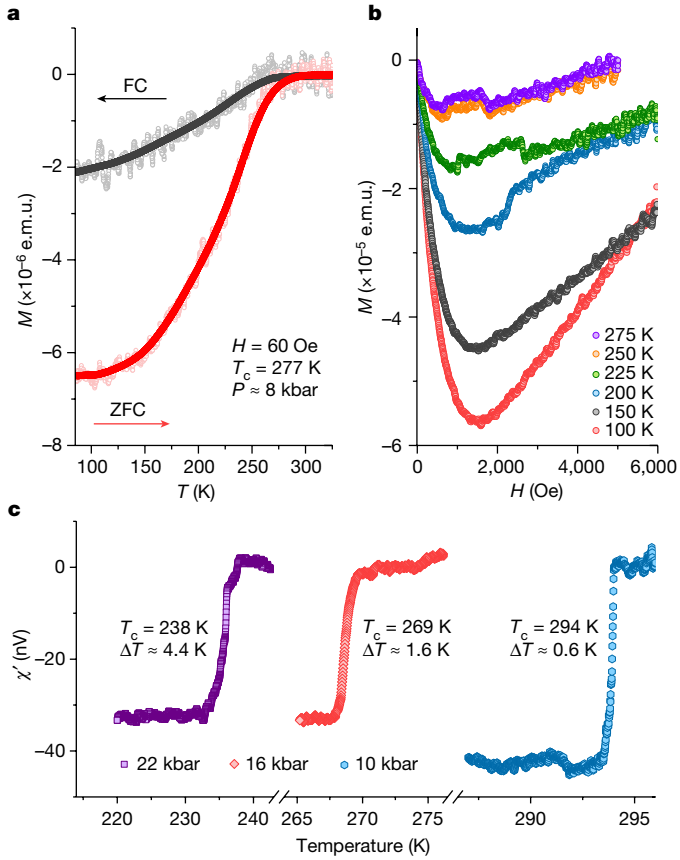

Fig. 3 | Magnetic susceptibility. a, Magnetic susceptibility ($\chi = M/H$, in which M is magnetization and H is magnetic field) as a function of temperature (T) under conditions of zero field cooling (ZFC) and field cooling (FC) at a d.c. field of 60 Oe. **b**, M–H curves recorded close to zero field. **c**, a.c. susceptibility (χ) in nanovolts versus temperature at select pressures, showing marked diamagnetic shielding of the superconducting transition for pressures of 10–22 kbar. The superconducting transition shifts rapidly under pressure to lower temperatures. T_c is determined from the temperature at the onset of the transition. A cubic or quadratic fit of the background signal has been subtracted from the data. We have applied a ten-point adjacent average smoothing for all d.c. magnetization data.

elemental analysis and EDX analysis on the synthesized sample at ambient pressures. The bulk material consistently shows the presence of nitrogen with an average weight percent of 0.8–0.9%N using elemental analysis. EDX, although qualitative, provides evidence of nitrogen in various domains of the overall sample, which we related to partial inhomogeneity in our samples (see Extended Data Fig. 7). The atomic arrangement of these elements is the crux of why the material superconducts, and both XRD and Raman spectroscopy (see Extended Data Fig. 1) show the presence of two distinct hydride compounds in nearly all samples. Both compounds have the same chemical construct of a face-centred cubic (fcc) metal sublattice but with varying contents of hydrogen and nitrogen and a distinct difference in colour. Compound A is indexed as $Fm\bar{3}m$ with a lattice constant of a = 5.0289(4) Å, whereas compound B has a = 4.7529(9) Å, both of which are indicative of lanthanoid hydride and nitride compounds, respectively[9,35,41,44] (Fig. 5a). The mononitride of lutetium is known and reported to adopt a rock-salt (RS) structure with a lattice constant of a = 4.76 Å (ref. [44]), very similar to what is measured here for compound B. DFT optimization of the RS and a hypothetical zincblende (ZB) mononitride yields a = 4.767 and 5.144 Å, respectively. In the same lattices, the hypothetical RS and ZB structure Lu monohydrides have DFT-optimized lattice constants of a = 4.800 and 5.027 Å, respectively. Altering the H and N concentration in the RS structure causes the lattice constant to vary between the limits set by the two parent compounds. Forming fully stoichiometric monohydrides and mononitrides is known to be difficult, so compound B is tentatively assigned as the RS mononitride with potential hydrogen substitution/intercalation, that is, $LuN_{1-\delta}H_{\varepsilon}$.

The electronic and structural evolutions of compound A are codependent and evolve synchronously. Raman spectroscopy of the starting material shows a linear-like progression with compression as modes harden associated with bond stiffening. A gradient change in the mode progression is observed above 3 kbar, in step with the onset of superconductivity in phase II (see Extended Data Fig. 1). There is no registered change in the indexed $Fm\bar{3}m$ symmetry as the phase I to phase II boundary is crossed, indicative of an isostructural second-order phase transition, at least in relation to the cation positions. Compressing phase II into non-superconducting phase III is a first-order structural phase transition with a roughly 0.3% volume discontinuity and a reduction in symmetry of the metal sublattice to the orthorhombic *Immm* space group. Diminishing quantum properties as the loss of the superconductivity can be associated with a sudden increase in the degrees of freedom associated with phonon propagation through the lattice, yet there is no pronounced change in the Raman spectra other than the expected hardening of modes with compression and the disappearance of one of the low-frequency modes.

At ambient, the dihydride is a blue compound that takes on the fluorite structure (CaF_2, a fcc metal sublattice and the hydrogens almost entirely occupying the tetrahedral interstices), with a lattice constant of 5.033 Å (refs. [45–48]). Although 5.033 Å is larger than what is measured here for compound A, the lanthanoid dihydrides including Lu form solid solutions, LnH_{2+x}, that contract the lattice with further hydrogen uptake[45,46,49,50]. The presence of impurities such as O or N enables LuH_{2+x} to take on extra hydrogen compared with purer metal samples, although that contraction is only 10% that of other Ln hydrides and not enough to explain the lattice constant observed for phase I of compound A (refs. [49,50]). The ambient trihydride adopts a hexagonal $P\bar{3}c1$ phase[51]; however, a cubic trihydride phase begins to form under compression around 12 GPa and is recoverable to ambient[52]. DFT optimizations of the cubic Lu dihydride and trihydride give a = 5.025 and 5.012 Å, respectively, and an alternative higher-energy model of the dihydride with 50% of the hydrogens occupying all the octahedral sites and the other 50% occupying the tetrahedral interstices as in the ZB structure gives a = 4.960 Å. The disagreement between the computed and experimental lattice constant for the dihydride allows an estimate for the error in the DFT lattice predictions, but—more importantly—the difference in the computed lattice constants corroborates the expected lattice contraction on increasing hydrogen content from the dihydride to the trihydride. We interpret the ZB monohydride structure having a nearly identical lattice constant to the dihydride to mean that little change in the lattice should be anticipated when occupying further tetrahedral interstices with H beyond the ZB structure. For N incorporation into the lattice, as opposed to in grain boundaries as in the studies on further H uptake in the dihydride[49,50], DFT predicts a = 4.949 Å for adding a single N at an octahedral interstice in the cubic dihydride lattice, $LuH_2N_{0.25}$, and a = 5.034 Å for complete N occupation of the octahedral sites, LuH_2N. In the cubic-trihydride structure, replacing a single H for a N gives a = 5.028 and 5.146 Å for octahedral and tetrahedral interstices, respectively, which reduces to a = 5.021 and 5.080 Å, respectively, if the single N replacement is in a 2 × 2 × 2 supercell of the primitive rhombohedral cell.

In the harmonic approximation, the dihydride is the only stoichiometric low-H cubic Lu hydride found to be dynamically stable at ambient pressure (see Extended Data Fig. 8). The temperature-dependent conductivity of ambient-pressure LuH_{2+x} is known[49,50,53] and electron–phonon calculations corroborate 0-kbar LuH_2 as non-superconducting with low values of λ = 0.189 and ω_{log} = 363 K. ZB LuH has a weak instability, with the acoustic phonons at X precluding a calculation of its

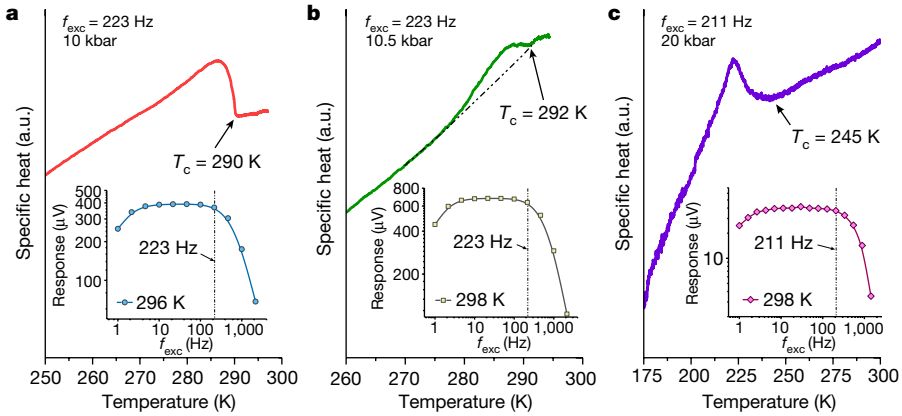

Fig. 4 | Specific-heat-capacity measurement on the superconducting lutetium–nitrogen–hydrogen system. a–c, Specific heat capacity of nitrogen-doped lutetium hydride at 10 kbar (**a**), 10.5 kbar (**b**) and 20 kbar (**c**), showing the superconducting transition as high as 292 K at 10.5 kbar in **b**. The drive frequency (f_{exc}) and frequency sweeps of each measurement are depicted in the insets. The strength of the heat-capacity anomaly associated with superconductivity varied owing to volume fraction as shown in **c**. The dashed line is a guide to the eye to distinguish the trend of the heat-capacity anomaly before and after the transition.

electron–phonon properties without a treatment for anharmonicity, but—because of the similarity between its and LuH_2's phonon band structure—we do not believe it to be a strong candidate for compound A. The larger harmonic dynamic instability at Γ in LuH_3 is a T_{1u} optical phonon mode that splits, with one branch becoming more unstable in other parts of the Brillouin zone. As this lattice could potentially be metastably recovered to ambient conditions[52,54], the stabilization of the material could also be attributed to anharmonic effects. Simulated compression to 15 GPa, at which LuH_3 has been observed experimentally, quenches the harmonic instabilities at the zone centre but not away from it, further indicating that anharmonicity plays a role in stabilizing cubic LuH_3 against the harmonic instabilities of the optical modes. An optical phonon mode of RS LuH also exhibits large harmonic dynamic instabilities, indicating that unstable optical modes arise from hydrogens in the octahedral fcc interstices. This observation is in line with neutron-diffraction results for cubic $NdD_{2.61}$, in which the D in the octahedral site shifts away from the 4b Wyckoff site to a partially occupied, lower-symmetry 32f site[55].

Single N substitution in the cubic cell of LuH_3 at both types of interstitial site increases the (harmonic) dynamic instability at Γ; however, they both split the highly degenerate zone-centred phonon modes of LuH_3, making more of them Raman active, in line with what is observed experimentally. Substitution at the tetrahedral site was found to be more enthalpically favourable than at the octahedral site (not vibrationally corrected), whereas Rietveld refinements provided similar patterns for N substitution at either site (see Extended Data Fig. 9). The LuH_2 to LuH_3 transformation is a metal to semimetal transition, wherein the Lu *d* electron driving the metallicity in LuH_2 donates to/interacts with the octahedral hydrogens in LuH_3, leading to a van Hove singularity[56] just below the Fermi level (see Extended Data Fig. 10). N incorporation at an octahedral interstice sees an increase in metallic character versus LuH_3, with the N p states being metallic, as well as an increased density of H states at the Fermi level. Conversely, N incorporation at a tetrahedral interstice drives the system into a semiconducting state. Although N is more electronegative than H, it does not go to N^{3-} in either case as N p states are in the conduction band, implying *M*–*N* covalencies. Also, N being more electronegative will prevent the formation of only H^- anions in the lattice, and H^- anions are known to be unfavourable for superconductivity. The primary reason for the difference in the electronic behaviours of the two types of substitution is that octahedral substitution has a minimal impact on the parent lattice, whereas tetrahedral substitution pushes the octahedral hydrogens into the opposite octant of the cube, similar to the packing seen in $LaBH_8$ (refs. [21,57,58]) (see Extended Data Fig. 11), which—in turn—leads to disordering of the Lu atoms and an approximately 0.12-Å expansion of the lattice distortions, well beyond what is measured by XRD. A lower N content suppresses the magnitude of the distortions seen for the tetrahedral substitution, and likewise its deviation away from metallicity, but not to the extent to provide a better match with experimental results as compared with octahedral substitution.

Preliminary investigations into adding H-vacancy defects into the cubic cell of the trihydride structure show that, as with the introduction of N, there is a varied response to the lattice, with the removal of an octahedral H giving a = 5.007 Å and the removal of a tetrahedral H giving a = 5.065 Å. These models both reduce in magnitude but do not remove the optical harmonic dynamic instability at Γ. As with N substitution, these structures split the phonon modes of the parent lattice at Γ, making many of them Raman active, such as what is observed experimentally. Considering that the ground-state structure of several of the ambient rare-earth trihydrides are hexagonal lattices, yet surface defects can metastably trap the high-pressure cubic phase down to ambient conditions as with YH_3 (ref. [54]), the anharmonicity of the hydrogenic phonons[59] along with a combination of N substitutions and H-vacancy defects are probably promoting the formation of a superconducting nitrogen-doped lutetium hydride with higher H content than the dihydride.

Discussion

Clearly, state-of-the-art experiments are needed to determine the exact crystal structure and stoichiometry of nitrogen-doped lutetium hydride and similar materials showing such high-temperature superconducting states. The use of techniques such as neutron diffraction and X-ray spectroscopy, as supported by simulations, are the most likely to provide a route to directly investigating the light elemental content of doped-metal hydrides and to build reliable atomistic descriptions of their chemical environments. A better detailed structural descriptor will enable theoretical modelling of these non-stoichiometric metal hydrides and improved theoretical understanding. An important distinction to make is that XRD was not satisfactorily authoritative for these hydrides even at ambient conditions, a shortcoming of such a technique that we have already highlighted in our work on carbonaceous sulfur hydride[14–16]. The fact that, in this study, we experience a lack of accuracy at ambient conditions confirms our concerns of using XRD techniques for determining hydrogen stoichiometry at more extreme conditions. The inability to accurately measure defect

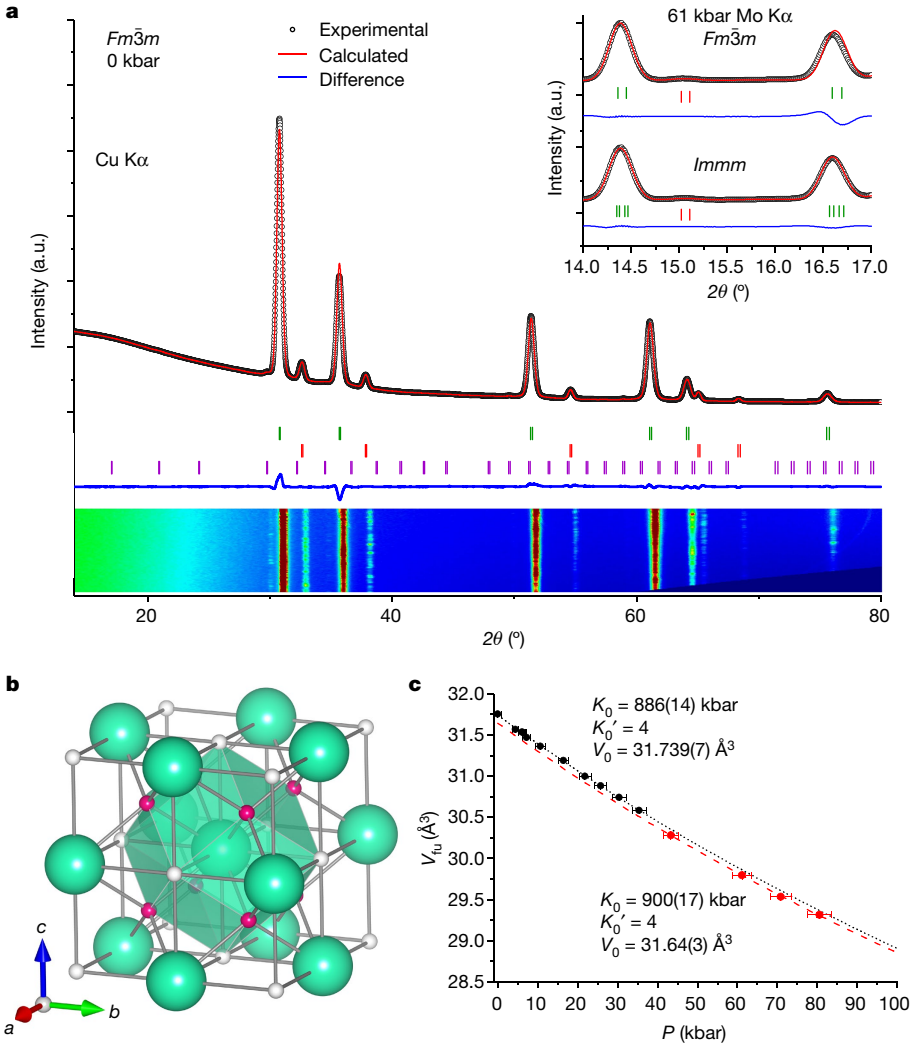

Fig. 5 | XRD studies of the superconducting lutetium–nitrogen–hydrogen system. a, Rietveld refinement of the X-ray powder diffraction data collected at 295 K with Cu Kα radiation. The black points, red line and blue line represent the observed data, calculated intensity and the difference between observed and calculated intensities, respectively. Green tick marks represent the expected Bragg peak positions for the main phase, which is probably $LuH_{3-\delta}N_{\varepsilon}$ (92.25%); minor phases, which are probably $LuN_{1-\delta}H_{\varepsilon}$ (7.29%) and Lu_2O_3 (0.46%), are shown as red and purple tick marks, respectively. The colour map is a cake representation of the X-ray powder diffraction data at ambient pressure. Insets show Le Bail fitting of high-pressure powder diffraction data at 61 kbar with the *Fm*$\bar{3}$*m* and *Immm* space groups. **b**, The crystal structure of the proposed $LuH_{3-\delta}N_{\varepsilon}$ phase. The hydrogens in octahedral interstitial sites are shown in white and those in tetrahedral interstitial sites are in pink. The lutetium atoms are in green and the coordination polyhedron is shown about the central Lu atom. The cell is shifted by (0.5, 0.5, 0.5) fractional coordinates from the standard setting to better represent the coordination polyhedron. **c**, The lattice constant as a function of pressure for the *Fm*$\bar{3}$*m* main phase. The Le Bail method was used for the refinement of the high-pressure XRD data. The equation of state was fitted using the Birch–Murnaghan method, as shown by the dashed lines for two pressure ranges, 0 kbar < P < 40 kbar (black) and P > 42.7 kbar (red), and the corresponding K_0 (bulk modulus at P = 0), V_0 (reference volume at P = 0) and K_0' (derivative of the bulk modulus with respect to pressure at P = 0) are shown.

densities and fractional occupancies of the lightest elements is mostly a consequence of extremely complex synthesis techniques and which in turn limits the accurate boundary conditions to aid theoretical methods for modelling and predicting the quantum properties of such materials. In summary, the most remarkable result of this study is the evidence for the near-ambient superconducting state observed in N-doped lutetium hydride with T_c of 294 K at 10 kbar. On the basis of the measured XRD and Raman spectra, the observed superconducting properties can most probably be attributed to *Fm*$\bar{3}$*m* $LuH_{3-\delta}N_{\varepsilon}$, for which different non-stoichiometric values are used to indicate the possibility of both N-substitution and H-vacancy defects. The physical properties of the superconducting N-doped lutetium hydride will be better constrained by magnetic-field-dependence resistance, susceptibility and heat-capacity measurements. Whilst all other high-temperature superconducting metal hydrides have been observed at multi-megabar pressure conditions, our discovery of a 21 °C superconducting material at 10 kbar will certainly lead to the emergence of a new field of materials science, as such conditions are substantially more accessible to a multitude of new researchers outside the field of high-pressure physics.

Online content

Any methods, additional references, Nature Portfolio reporting summaries, source data, extended data, supplementary information, acknowledgements, peer review information; details of author contributions and competing interests; and statements of data and code availability are available at https://doi.org/10.1038/s41586-023-05742-0.

1. Onnes, H. K. The resistance of pure mercury at helium temperatures. *Commun. Phys. Lab. Univ. Leiden* **12**, 120 (1911).
2. Ginzburg, V. L. Nobel Lecture: On superconductivity and superfluidity (what I have and have not managed to do) as well as on the "physical minimum" at the beginning of the XXI century. *Rev. Mod. Phys.* **76**, 981–998 (2004).
3. Bednorz, J. G. & Müller, K. A. Possible high T_c superconductivity in the Ba–La–Cu–O system. *Z. Phys. B Condens. Matter* **64**, 189–193 (1986).
4. Wu, M. K. et al. Superconductivity at 93 K in a new mixed-phase Y-Ba-Cu-O compound system at ambient pressure. *Phys. Rev. Lett.* **58**, 908–910 (1987).
5. Schilling, A., Cantoni, M., Guo, J. D. & Ott, H. R. Superconductivity above 130 K in the Hg–Ba–Ca–Cu–O system. *Nature* **363**, 56–58 (1993).
6. Carlsson, A. E. & Ashcroft, N. W. Approaches for reducing the insulator-metal transition pressure in hydrogen. *Phys. Rev. Lett.* **50**, 1305–1308 (1983).
7. Ashcroft, N. W. Hydrogen dominant metallic alloys: high temperature superconductors? *Phys. Rev. Lett.* **92**, 187002 (2004).
8. Liu, H., Naumov, I. I., Hoffmann, R., Ashcroft, N. W. & Hemley, R. J. Potential high-T_c superconducting lanthanum and yttrium hydrides at high pressure. *Proc. Natl Acad. Sci.* **114**, 6990–6995 (2017).
9. Peng, F. et al. Hydrogen clathrate structures in rare earth hydrides at high pressures: possible route to room-temperature superconductivity. *Phys. Rev. Lett.* **119**, 107001 (2017).
10. Drozdov, A. P. et al. Superconductivity at 250 K in lanthanum hydride under high pressures. *Nature* **569**, 528–531 (2019).
11. Somayazulu, M. et al. Evidence for superconductivity above 260 K in lanthanum superhydride at megabar pressures. *Phys. Rev. Lett.* **122**, 27001 (2019).
12. Snider, E. et al. Synthesis of yttrium superhydride superconductor with a transition temperature up to 262 K by catalytic hydrogenation at high pressures. *Phys. Rev. Lett.* **126**, 117003 (2021).
13. Troyan, I. A. et al. Anomalous high-temperature superconductivity in YH_6. *Adv. Mater.* **33**, 2006832 (2021).
14. Snider, E. et al. Retraction article: Room-temperature superconductivity in a carbonaceous sulfur hydride. *Nature* **586**, 373–377 (2020).
15. Snider, E. et al. Retraction note: Room-temperature superconductivity in a carbonaceous sulfur hydride. *Nature* **610**, 804 (2022).
16. Smith, G. A. et al. Carbon content drives high temperature superconductivity in a carbonaceous sulfur hydride below 100 GPa. *Chem. Commun.* **58**, 9064–9067 (2022).
17. Sun, Y., Lv, J., Xie, Y., Liu, H. & Ma, Y. Route to a superconducting phase above room temperature in electron-doped hydride compounds under high pressure. *Phys. Rev. Lett.* **123**, 097001 (2019).
18. Ge, Y., Zhang, F. & Hemley, R. J. Room-temperature superconductivity in boron- and nitrogen-doped lanthanum superhydride. *Phys. Rev. B* **104**, 214505 (2021).
19. Grockowiak, A. D. et al. Hot hydride superconductivity above 550 K. *Front. Electron. Mater.* **2**, 837651 (2022).
20. Zhang, Z. et al. Design principles for high-temperature superconductors with a hydrogen-based alloy backbone at moderate pressure. *Phys. Rev. Lett.* **128**, 047001 (2022).
21. Di Cataldo, S., Heil, C., von der Linden, W. & Boeri, L. $LaBH_8$: towards high-T_c low-pressure superconductivity in ternary superhydrides. *Phys. Rev. B* **104**, L020511 (2021).
22. Ashcroft, N. W. Metallic hydrogen: a high-temperature superconductor? *Phys. Rev. Lett.* **21**, 1748 (1968).
23. Richardson, C. F. & Ashcroft, N. W. High temperature superconductivity in metallic hydrogen: electron-electron enhancements. *Phys. Rev. Lett.* **78**, 118–121 (1997).
24. Dias, R. P. & Silvera, I. F. Observation of the Wigner-Huntington transition to metallic hydrogen. *Science* **355**, 715–718 (2017).
25. Loubeyre, P., Occelli, F. & Dumas, P. Synchrotron infrared spectroscopic evidence of the probable transition to metal hydrogen. *Nature* **577**, 631–635 (2020).
26. Wang, H., Tse, J. S., Tanaka, K., Iitaka, T. & Ma, Y. Superconductive sodalite-like clathrate calcium hydride at high pressures. *Proc. Natl Acad. Sci.* **109**, 6463–6466 (2012).
27. Drozdov, A. P., Eremets, M. I., Troyan, I. A., Ksenofontov, V. & Shylin, S. I. Conventional superconductivity at 203 kelvin at high pressures in the sulfur hydride system. *Nature* **525**, 73–76 (2015).
28. Bi, T., Zarifi, N., Terpstra, T. & Zurek, E. in *Reference Module in Chemistry, Molecular Sciences and Chemical Engineering* (Elsevier, 2019).
29. Hilleke, K. P. & Zurek, E. Tuning chemical precompression: theoretical design and crystal chemistry of novel hydrides in the quest for warm and light superconductivity at ambient pressures. *J. Appl. Phys.* **131**, 070901 (2022).
30. Di Cataldo, S., von der Linden, W. & Boeri, L. First-principles search of hot superconductivity in La-*X*-H ternary hydrides. *npj Comput. Mater.* **8**, 2 (2022).
31. Di Cataldo, S., Qulaghasi, S., Bachelet, G. B. & Boeri, L. High-T_c superconductivity in doped boron-carbon clathrates. *Phys. Rev. B* **105**, 064516 (2022).
32. Ye, X., Zarifi, N., Zurek, E., Hoffmann, R. & Ashcroft, N. W. High hydrides of scandium under pressure: potential superconductors. *J. Phys. Chem. C* **122**, 6298–6309 (2018).
33. Shannon, R. D. Revised effective ionic radii and systematic studies of interatomic distances in halides and chalcogenides. *Acta Crystallogr. A* **32**, 751–767 (1976).
34. Rumble, J. R. (ed.) *CRC Handbook of Chemistry and Physics* 102nd edn (CRC Press/Taylor & Francis, 2021).
35. Greenwood, N. N. & Earnshaw, A. (eds) *Chemistry of the Elements* 2nd edn (Butterworth-Heinemann, 1997).
36. Zhou, D. et al. Superconducting praseodymium superhydrides. *Sci. Adv.* **6**, 6849–6877 (2020).
37. Zhou, D. et al. High-pressure synthesis of magnetic neodymium polyhydrides. *J. Am. Chem. Soc.* **142**, 2803–2811 (2020).
38. Semenok, D. V. et al. Effect of magnetic impurities on superconductivity in LaH_{10}. *Adv. Mater.* **34**, 2204038 (2022).
39. Sun, W., Kuang, X., Keen, H. D. J., Lu, C. & Hermann, A. Second group of high-pressure high-temperature lanthanide polyhydride superconductors. *Phys. Rev. B* **102**, 144524 (2020).
40. Jaroń, T. et al. Synthesis, structure, and electric conductivity of higher hydrides of ytterbium at high pressure. *Inorg. Chem.* **61**, 8694–8702 (2022).
41. Song, H. et al. High T_c superconductivity in heavy rare earth hydrides. *Chin. Phys. Lett.* **38**, 107401 (2021).
42. Cornelius, A. L., Lawler, K. V. & Salamat, A. Understanding hydrogen rich superconductors: importance of effective mass and dirty limit. Preprint at https://doi.org/10.48550/arxiv.2202.04254 (2022).
43. Dasenbrock-Gammon, N., McBride, R., Yoo, G., Dissanayake, S. & Dias, R. Second harmonic AC calorimetry technique within a diamond anvil cell. *Rev. Sci. Instrum.* **93**, 093901 (2022).
44. Klesnar, H. P. & Rogl, P. Phase relations in the ternary systems rare-earth metal (RE)-boron-nitrogen, where RE = Tb, Dy, Ho, Er, Tm, Lu, Sc and Y. *High Temp. High Press.* **22**, 453–457 (1990).
45. Pebler, A. & Wallace, W. E. Crystal structures of some lanthanide hydrides. *J. Phys. Chem.* **66**, 148–151 (1962).
46. Bonnet, J. E. & Daou, J. N. Rare-earth dihydride compounds: lattice thermal expansion and investigation of the thermal dissociation. *J. Appl. Phys.* **48**, 964–968 (1977).
47. Weaver, J. H., Rosei, R. & Peterson, D. T. Electronic structure of metal hydrides. I. Optical studies of ScH_2, YH_2, and LuH_2. *Phys. Rev. B* **19**, 4855–4866 (1979).
48. Peterman, D. J., Harmon, B. N., Marchiando, J. & Weaver, J. H. Electronic structure of metal hydrides. II. Band theory of ScH_2 and YH_2. *Phys. Rev. B* **19**, 4867–4875 (1979).
49. Daou, J. N., Vajda, P., Burger, J. P. & Shaltiel, D. Percolating electrical conductivity in two phased LuH_{2+x} compounds. *Europhys. Lett.* **6**, 647–651 (1988).
50. Daou, J. N., Vajda, P., Burger, J. P. & Shaltiel, D. Percolating electrical conductivity in two phased LuH2+x compounds. *Europhys. Lett.* **8**, 587 (1989).
51. Mansmann, M. & Wallace, W. E. The structure of HoD3. *J. Phys.* **25**, 454–459 (1964).
52. Palasyuk, T. & Tkacz, M. Pressure-induced structural phase transition in rare-earth trihydrides. Part I. (GdH_3, HoH_3, LuH_3). *Solid State Commun.* **133**, 481–486 (2005).
53. Daou, J. N., Lucasson, A., Vajda, P. & Burger, J. P. Observation of the optical and acoustic electron-phonon coupling in Sc, Y and Lu dihydrides and dideuterides by electrical resistivity. *J. Phys. F Metal Phys.* **14**, 2983–2993 (1984).
54. Kataoka, R. et al. The origin of the highly crystallized face-centered cubic YH_3 high-pressure phase when quenched to ambient condition. *Mater. Today Commun.* **31**, 103265 (2022).
55. Renaudin, G., Fischer, P. & Yvon, K. Neodymium trihydride, NdH_3, with tysonite type structure. *J. Alloys Compd.* **313**, L10–L14 (2000).
56. Villa-Cortés, S. & De la Peña-Seaman, O. Effect of van Hove singularity on the isotope effect and critical temperature of H_3S hydride superconductor as a function of pressure. *J. Phys. Chem. Solids* **161**, 110451 (2022).
57. Liang, X. et al. Prediction of high-T_c superconductivity in ternary lanthanum borohydrides. *Phys. Rev. B* **104**, 134501 (2021).
58. Belli, F. & Errea, I. Impact of ionic quantum fluctuations on the thermodynamic stability and superconductivity of. *Phys. Rev. B* **106**, 134509 (2022).
59. Errea, I. Superconducting hydrides on a quantum landscape. *J. Phys. Condens. Matter* **34**, 231501 (2022).

Publisher's note Springer Nature remains neutral with regard to jurisdictional claims in published maps and institutional affiliations.

Springer Nature or its licensor (e.g. a society or other partner) holds exclusive rights to this article under a publishing agreement with the author(s) or other rightsholder(s); author self-archiving of the accepted manuscript version of this article is solely governed by the terms of such publishing agreement and applicable law.

© The Author(s), under exclusive licence to Springer Nature Limited 2023

Methods

High-pressure experiments

This study was based on a large number of experiments, with more than a hundred samples. The samples were loaded onto a membrane-driven diamond anvil cell (m-DAC), using 1/3-carat, type Ia diamond anvils with a 0.2-mm, 0.4-mm, 0.6-mm and 0.8-mm (for low pressures) culet. A 0.25-mm-thick rhenium gasket was pre-indented to 15–100 μm (depending on the pressure and experiment) and a 120-μm hole (or 280 μm or 600 μm for low pressures) was electrospark drilled at the centre of the gasket. We used a high-pressure gas loader to compress gasses to high densities. The m-DACs were first loosely closed and mounted into a gearbox. The DAC and gearbox were then placed into a high-pressure gas loader (Top Industries). The system was first flushed with gasses to purge the circuit of impurities and then the sample chamber was pressurized. A 100-μm Lu foil was compressed between two diamonds to make it thinner than 100 μm and then loaded into a DAC with the H_2/N_2 gas mixture (99:1) and pressed to 2 GPa. We have not used any other gas ratios in our synthesis. All of the prepared samples were kept in a glovebox, closed and reopened to load with gas in a pre-purged hydrogen-rich environment. The glovebox environment was operated at levels at which O_2 and H_2O were each less than 0.5 ppm. The sample was heated in an oven overnight at 65 °C. After 24 h, the DAC was released to recover the sample. The samples were characterized using Raman and XRD studies. We have also used commercially available LuH_2/LuH_3. Owing to extremely complex synthesis techniques, controlling the correct stoichiometry with the right amount of hydrogen and nitrogen percentages was extremely challenging. The success rate of measuring a sample with superconducting properties was about 35%.

Raman spectroscopy, pressure and temperature determination

Raman spectroscopy was carried out using a custom micro-Raman setup in back-scattering geometry, along with Bragg notch filters, using a 532-nm Millennia eV laser, a Princeton Instruments HRS-500 spectrometer and a Pylon camera. Pressure determination was predominantly carried out using ruby fluorescence with the pressure gauge of Shen et al.[60] and the temperature correction of Datchi et al.[61]. Furthermore, pressure was also measured from the observed Raman peak location following several calibrations runs to determine the pressure dependence of the Raman modes. Pressure was measured during both cooling and heating. DT-670 silicon diodes were used to measure the temperature to five digits with our temperature controller (that is, two decimal places above 100 K or three decimal places below 100 K). The temperature uncertainty is larger than that precision as the diodes cannot be placed directly on the sample in a DAC and are placed outside the sample chamber and on the mechanical assembly around the DAC. Thus, the temperature uncertainty is dominated by thermal gradients between the temperature probes and the sample in the DAC, which are large while cooling down but much smaller while warming owing to the associated cooling and warming rates.

Electrical-resistance measurements

The resistance measurements were performed using standard DAC techniques with a standard four-probe technique similar to Dias et al.[62] that was used to measure the resistance of the sample. Either Al_2O_3 or diamond powder was packed into an insulating shell in which sample is loaded. Platinum foil (5 μm in thickness) cut electrodes are placed in contact with the sample, leading out of the pressure cell, allowing for transport measurements of the samples under pressure. Electrical resistance is thus measured in a four-probe configuration. The resistance measured on both warming and cooling at about 10 kbar is shown in Extended Data Fig. 13. A Keithley 6221 current source is used to apply a low-frequency (13 or 17 Hz) current across two of the probes and a SR860 lock-in amplifier with a 500× preamplifier measures the resulting voltage across the remaining two probes. For relatively high (on the order of about kΩ or more) resistance samples, a d.c. configuration is used, whereby a d.c. current is applied across two of the probes using a SRS CS580 current source, whereas the resulting voltage on the remaining two probes is measured with a DMM6500. In some cases, small residual resistance from the instrument offsets was subtracted from the measured voltage. We used a custom-built BeCu DAC for magnetic-field-dependent electrical-resistance studies using a custom-designed magnet from ColdEdge Inc. The V–I curves were obtained by supplying an a.c. current between 0 and 4 mA across the sample and measuring the voltage response, at temperatures above and below the critical temperature T_c. Above T_c, a current sweep from 0 to 4 mA was performed in 50 equally spaced steps and a linear response in the V–I curve is observed.

a.c. calorimetry measurements

For measurement of the specific heat capacity, a modified version of the conductivity setup is used[43]. Two sets of two probes are shorted in contact with the sample. The first, Ti, nichrome or Pt, serves as the heater. The second uses a pair of materials with differing Seebeck coefficients, either Pt/Ag or the standard alumel/chromel thermocouple pair. Typically, a NaCl insulating insert was used to isolate the sample better thermally. Extended Data Fig. 2, top shows the schematic representation of the setup and Extended Data Fig. 2, bottom shows the actual setup in the DAC.

To make measurements, the heater is driven at frequency f (typically between 50 and 500 Hz). The sample is thus ohmically heated and modulated at frequency $2 \times f$. Then the DAC is externally cooled or heated and the voltage measured across the thermocouple, using a lock-in amplifier reading at frequency $2 \times f$, which was shown to inversely proportional to the specific heat of the sample at any given temperature[63]. To verify appropriate behaviour, both current and frequency sweeps of the drive are performed, as shown in Extended Data Fig. 3. Frequency dependence is shown to exhibit a characteristic dome shape with a wide plateau, and the current sweep shows a quadratic dependence, as expected from ohmic heating. For this type of a.c. calorimetric measurements, the governing equation is given by[63]: $C_{\mathrm{a.c}} = \frac{P}{\omega T_{\mathrm{a.c.}}} F(\omega)$, with $C_{\mathrm{a.c.}}$ being the a.c. heat capacity, P the driving power, ω the driving frequency, $T_{\mathrm{a.c.}}$ the modulation in temperature of the sample and $F(\omega)$ the frequency response curve. The details of the frequency response curve are described elsewhere[63,64] but it depends on the relation between the three timescales of the system: $\tau_1 = 1/\omega_1$ is the timescale over which the sample thermalizes with the environment, that is, how fast heat dissipates from the sample to the NaCl in which the sample is sitting; $\tau_2 = 1/\omega_2$ is the timescale over which the heater, sample and thermocouple thermalize with each other; and $\tau_3 = 1/\omega_3$ is the timescale of the driving heater. The first two timescales, ω_1 and ω_2, are determined by the exact details of the experimental setup and will vary between runs, although care is taken so that $\omega_1 < \omega_2$ and the sample is able to thermalize with the heater and thermocouple before heat dissipates into the environment. This is accomplished by using the thermally insulating NaCl medium.

The third timescale is chosen by the frequency of the driving current and is an experimental parameter. Before performing an experiment, care is taken so that an appropriate driving frequency, or ω_3, is chosen. This is best seen by performing a frequency sweep of the drive, as shown in Extended Data Fig. 3, and shows the frequency response curve, $F(\omega)$. The response falls into three regions: an initial rise, a flat plateau and a final decline. The first region corresponds to $\omega_3 \ll \omega_1$; low-frequency drive results in heat dissipating to the environment, reducing the change in temperature of the sample. The third region corresponds to $\omega_3 \gg \omega_2$; the sample is not able to thermalize with the heater/thermocouple because the drive is too fast. The intermediate plateau between these two regions is where the response function is relatively constant with frequency, and there is good coupling between the heater, sample and thermocouple, with minimized loss to the environment. The final consideration is experimental. By using higher

frequencies, the signal-to-noise ratio is improved and so a frequency between regions two and three is typically chosen.

Because the heater is driven at frequency f, the sample will experience temperature oscillations at frequency $2 \times f$ and the thermocouple will produce a voltage at $2 \times f$. The heat capacity is then inversely proportional to the measured voltage. As extra verification, a current sweep is performed to make sure the expected quadratic behaviour is produced, as shown in Extended Data Fig. 3, inset. A current is chosen at which acceptable signal is measured, but high currents are avoided to minimize d.c. heating that may occur on the sample. An example measurement and frequency sweep are shown in Extended Data Fig. 4.

a.c. magnetic-susceptibility measurements

All experiments were performed using a side-by-side double-coil technique as described by Debessai et al.[65]. In a single-coil setup, the measured voltage will be proportional to the average magnetic susceptibility of the volume contained in the coil. Owing to the geometry of the diamonds used within a DAC, the sample is necessarily a small fraction of the volume contained in the coil. We therefore use a double-coil setup whereby a second coil is connected in series but reversed relative to the first coil. We call the coil surrounding the sample the 'primary' coil and the second coil the 'dummy' coil. When connected in reverse, the signal from both coils essentially subtracts. Because the coils are near identical, when subtracted, the remaining difference should be because of the sample. In practice, the coils are never perfectly identical. The coils are hand wound in house to be as identical as possible, before being balanced for use in an experiment. To balance a pair of coils, first the pickup from the primary coil is measured and then the second coil is connected in reverse. While monitoring the pickup, one of the coils is slowly unwound until the measured pickup is as small as possible. The balancing is done until the signal is less than 1% of the single-coil reference value and most coils are balanced to 0.1–0.5%. This residual signal is what is measured as the (relatively) large background as compared with the signal strength coming from the sample. For improved resolution of the small signal voltages, a 500× preamplifier (SR554 Transformer Preamplifier) is often used. After dividing out the 500× preamplifier, the signal strengths are in the range of approximately 10–200 nV, depending on the sample and conditions. Owing to the small sample size, a large temperature-dependent background signal is observed, but the transition is clearly visible despite the large magnitude of the background. A background must be subtracted from the real part, yielding the final susceptibility signal. In this work, cubic or quadratic polynomial backgrounds were used (Extended Data Fig. 5), taking the measured voltage either immediately before or immediately after the transition.

d.c. magnetic susceptibility

We used the non-membrane-driven clamp-style pressure cell manufactured by HMD, a leading Japanese supplier of pressure cells for magnetometry. A schematic and actual picture of the HMD-13 cell can be found in the cell manual. This simplified design requires neither copper sealing rings nor a hydraulic press to achieve the pressure. The HMD-13 cell is designed with a BeCu construction and affords a minimized, uniform magnetic background, typically 4×10^{-7} e.m.u. gauss^{-1}. This pressure cell is a clamp cell, in which the sample is loaded with Daphne 7373 pressure medium inside a Teflon tube and closed using a Teflon capsule. Measurements were performed by directly measuring the HMD cell, which does not require a diamond or gasket. The samples that we use for this measurement are much larger compared with the DAC measurements. We have loaded large (approximately 150 μm × 100 μm) pieces into the Teflon capsule. The sample centre is known from the dimensions and pressure-cell compression, which is very standard in these experiments. The magnetization measurement was performed using a VSM option. The VSM option includes a linear motor transport for vibrating the sample, a coil set and the software application. An empty cell without the sample while keeping everything else the same was also performed to identify the cell background. The empty cell background is mostly constant with temperature. A linear or cubic background response was subtracted from the data, and we have applied a ten-point adjacent-average smoothing for all of the data (see Extended Data Fig. 14). The HMD-13 high-pressure cell is rated to reach a maximum pressure of up to 13 kbar. To achieve the highest pressure rated for this cell, the Teflon sample tube should be filled with as much sample as possible, with the minimum amount of pressure-transmitting medium required to fill the Teflon sample chamber. If the filling factor of the sample is small (limited by the synthesis procedure), achieving the rated pressure of 10 kbar will require substantially greater pressure-cell compression.

XRD and elemental analysis

For ambient X-ray powder diffraction measurements, microgram polycrystalline samples with typical sizes ($0.07 \times 0.05 \times 0.02$ mm^3) were placed onto a nylon loop and mounted in a Rigaku XtaLAB Synergy-S Dualflex diffractometer equipped with a HyPix-6000HE Hybrid X-ray Photon Counting area detector. The full data collection was carried out using a PhotonJet (Cu Kα) X-ray source with a detector distance of 34.0 mm. Data collection was performed using Gandolfi scans, which randomize the sample orientation in the beam by driving both phi and omega circles simultaneously. The scans were repeated for different kappa settings. CrysAlis Pro software was used to process and evaluate powder measurements. The Rietveld refinements of the ambient XRD data were performed using FullProf. High-pressure XRD measurements were performed using the Rigaku high-pressure kit designed for the Rigaku XtaLAB Synergy-S Dualflex diffractometer. Pressure was generated in custom-made PEAS-Q36 DACs. Two-hundred-micrometre conical diamonds were mounted on tungsten carbide bases with 70° opening angle. Data collection was carried out using a PhotonJet (Mo Kα) X-ray source with a detector distance of 80 mm. Samples were placed into either a rhenium or a tungsten gasket with a glycerine or methanol/ethanol pressure medium. Ag pieces (roughly 20 × 20 μm) were placed with the samples as a pressure marker. Pressure was estimated using the equation of state of Ag at 295 K. The pressure dependence of the lattice parameters was obtained from Le Bail refinement for the high-pressure XRD data using FullProf.

Elemental analysis was carried out using a PerkinElmer 2400 Series II CHNS/O Elemental Analyzer instrument for rapid determination of the carbon, hydrogen and nitrogen content in our samples. The instrument uses a helium carrier gas with an accuracy of about 0.3% for each element. The samples are crimp-sealed in special tin capsules before being loaded and burned in the instrument. Several different samples were prepared in an Ar glovebox to compare the elemental analysis results with samples that were prepared in air. Similar N content was detected in the samples tested in Ar atmosphere and air.

Simulations

Plane-wave DFT simulations using the Perdew–Burke–Ernzerhof[66] generalized gradient approximation functional were performed with Quantum ESPRESSO[67,68]. The convergence threshold for self-consistent field energies was 10^{-13} Ry, the convergence for forces was 10^{-6} Ry Bohr^{-1} and the stress convergence was 10^{-3} kbar. Gaussian smearing was used with a smearing width of 0.015 Ry. The phonons of cubic unit cells were calculated on $4 \times 4 \times 4$ $\vec{q}$-grids and those of rhombohedral primitive cells were calculated on $6 \times 6 \times 6$ $\vec{q}$-grids. Rhombohedral primitive cells were used whenever possible. The $\vec{k}$-grid density for the structural optimizations and phonon simulations was double that of the $\vec{q}$-grid in each direction, and the denser $\vec{k}$-grid for electron–phonon couplings was four times as dense as the $\vec{q}$-grid in each direction. In all visualizations and electron–phonon calculations, the 'simple' acoustic sum rule correction implemented in Quantum ESPRESSO was applied to the computed phonons. The PseudoDojo norm-conserving pseudopotentials were used with a kinetic energy cutoff of 100 Ry and charge density cutoff of 400 Ry (ref. [69]). Norm-conserving pseudopotentials were used

to perform the electron–phonon calculations, along with a simplified Hubbard correction (DFT+U) applied to the *f* electrons[70,71]. A Hubbard U of 5.5 eV was selected in a similar fashion to the pseudopotential formulation of Topsakal and Wentzcovitch[72], that is, comparing the optimized lattice constants of the metal mononitride to experiment on a 0.5-eV interval. Those pseudopotentials were not used because they are at present incompatible with Quantum ESPRESSO density functional perturbation theory phonon calculations with a +U correction. The importance of describing the *f* electrons with DFT+U was tested by performing structural optimizations with the *f* electrons in core (using the pslibrary[73] PAW[74] pseudopotential for the metal) and with no Hubbard correction applied. In both of those cases, we found the lattice constants of all evaluated compounds to be underestimated compared with the available literature and experimental results. Neither of those two approaches were found to eliminate the dynamic instabilities of the trihydride (Extended Data Fig. 8b), although the instability at Γ was reduced in magnitude with the *f* electrons placed in core. To explore the dynamic instability of the trihydride, the displacements of NdD_3 (ref. [55]) were tested, as well as adding noise to each H position in the cubic unit cell in line with the displacements along one of the unstable optical phonon modes at Γ. The resulting structure was lower in energy and determined to be of the *Pmnm* space group, a subgroup of the XRD-determined *Immm* phase III structure (Extended Data Fig. 11b). Substitution of a N into a tetrahedral site of the distorted cubic representation of the *Pmnm* structure strongly reduced the distortions away from cubic (that is, cell edges that differ by less than 0.001 Å rather than 0.640 Å). The lighter lanthanoid hydrides $LnH(D)_x$ are known to tetragonally distort above $x \geq 2.3$ (refs. [75,76]), so it is possible that the phase II to III transformation is driven by the harmonic dynamic instabilities of the cubic trihydride. As there is no other hydrogen present and the transformation into phase III is recoverable to phase I, it is not likely that the sample is undergoing disproportionation to form a variant of the predicted tetragonal LuH_4 lattice[41].

It should be noted that LuH_2 has a particularly low uncorrected acoustic phonon frequency of about −110 cm^{-1} at Γ, which is not improved by doubling the size of the $\vec{k}$-grid in each direction or increasing the wavefunction cutoff. We found that, instead of representing the primitive cell of LuH_2 with the more highly symmetric lattice vectors of a fcc system, using a triclinic representation with x along a and z along c^* (which uses a D_3 electronic point group as opposed to O_h) has a negligible effect on the optimized lattice but alleviates the very negative uncorrected frequency at Γ. However, this creates weak dynamic instabilities of the acoustic phonons just off of Γ (see Extended Data Fig. 8), implying that anharmonic contributions may play a role in stabilizing the lattice, similar to how they were found to stabilize $Im\bar{3}m$ H_3S below 175 GPa (ref. [77]). Changing between the triclinic or more symmetric representation of the primitive unit cell's lattice vectors does not alleviate the optical dynamic instabilities of LuH_3. In addition, the phonon band dispersions for LuH_2 and ZB LuH in the highly symmetric lattice vectors were evaluated as a function of pressure up to 50 kbar. However, no notable change to their phonon band structures was observed, including the instability at X for ZB LuH (Extended Data Fig. 16).

Data availability

The authors declare that the data supporting the findings of this study are available in the article and its supplementary information files and from the public link https://doi.org/10.5281/zenodo.7374510. Source data are provided with this paper.

60. Shen, G. et al. Toward an international practical pressure scale: a proposal for an IPPS ruby gauge (IPPS-Ruby2020). *High Press. Res.* **40**, 299–314 (2020).
61. Datchi, F. et al. Optical pressure sensors for high-pressure–high-temperature studies in a diamond anvil cell. *High Press. Res.* **27**, 447–463 (2007).
62. Dias, R. P., Yoo, C.-S., Kim, M. & Tse, J. S. Insulator-metal transition of highly compressed carbon disulfide. *Phys. Rev. B* **84**, 144104 (2011).
63. Li, Y.-S., Borth, R., Hicks, C. W., Mackenzie, A. P. & Nicklas, M. Heat-capacity measurements under uniaxial pressure using a piezo-driven device. *Rev. Sci. Instrum.* **91**, 103903 (2020).
64. Kraftmakher, Y. *Modulation Calorimetry. Theory and Applications* (Springer, 2004).
65. Debessai, M., Hamlin, J. J. & Schilling, J. S. Comparison of the pressure dependences of T_c in the trivalent *d*-electron superconductors Sc, Y, La, and Lu up to megabar pressures. *Phys. Rev. B* **78**, 064519 (2008).
66. Perdew, J. P., Burke, K. & Ernzerhof, M. Generalized gradient approximation made simple. *Phys. Rev. Lett.* **77**, 3865–3868 (1996).
67. Giannozzi, P. et al. QUANTUM ESPRESSO: a modular and open-source software project for quantum simulations of materials. *J. Phys. Condens. Matter* **21**, 395502 (2009).
68. Giannozzi, P. et al. Advanced capabilities for materials modelling with Quantum ESPRESSO. *J. Phys. Condens. Matter* **29**, 465901 (2017).
69. van Setten, M. J. et al. The PseudoDojo: training and grading a 85 element optimized norm-conserving pseudopotential table. *Comput. Phys. Commun.* **226**, 39–54 (2018).
70. Dudarev, S. L., Botton, G. A., Savrasov, S. Y., Humphreys, C. J. & Sutton, A. P. Electron-energy-loss spectra and the structural stability of nickel oxide: an LSDA+U study. *Phys. Rev. B* **57**, 1505–1509 (1998).
71. Cococcioni, M. & de Gironcoli, S. Linear response approach to the calculation of the effective interaction parameters in the LDA+U method. *Phys. Rev. B* **71**, 035105 (2005).
72. Topsakal, M. & Wentzcovitch, R. M. Accurate projected augmented wave (PAW) datasets for rare-earth elements (RE = La–Lu). *Comput. Mater. Sci.* **95**, 263–270 (2014).
73. Dal Corso, A. Pseudopotentials periodic table: from H to Pu. *Comput. Mater. Sci.* **95**, 337–350 (2014).
74. Blöchl, P. E. Projector augmented-wave method. *Phys. Rev. B* **50**, 17953–17979 (1994).
75. Peterman, D. J., Weaver, J. H. & Peterson, D. T. Electronic structure of metal hydrides. V. *x*-dependent properties of LaH_x (1.9 < ~*x* < 2.9) and NdH_x (2.01 < ~*x* < ~2.27). *Phys. Rev. B* **23**, 3903–3913 (1981).
76. Knappe, P., Müller, H. & Mayer, H. W. Tetragonal rare earth hydrides $REH(D)_{<2.33}$ (RE = La, Ce, Pr, Nd, Sm) and a neutron diffraction study of $NdD_{2.36}$. *J. Less Common Metals* **95**, 323–333 (1983).
77. Errea, I. et al. Quantum hydrogen-bond symmetrization in the superconducting hydrogen sulfide system. *Nature* **532**, 81–84 (2016).

Acknowledgements We thank B. Brennessel from the Department of Chemistry at the University of Rochester for providing the technical assistance during the XRD and elemental analysis. We thank M. Debessai for his assistance on the coil setup for the magnetic-susceptibility measurements. Also, we thank I. Silvera and I. Hogarth for the useful scientific discussions and R. C. Heist and L. Koelbl for reading through the manuscript and providing valuable suggestions. Preparation of diamond surfaces and EDX measurements were performed in part at the University of Rochester Integrated Nanosystems Center. Computational resources were provided by the Center for Integrated Research Computing at the University of Rochester. This research was supported by NSF grant no. DMR-2046796, Unearthly Materials Inc. and US Department of Energy, Office of Science, Fusion Energy Sciences under award number DE-SC0020340.

Author contributions N.D.-G., E.S., R.M. and H.P. contributed equally to this work as co-first authors. E.S., D.D., N.D.-G., R.M., H.P. and R.P.D. contributed to performing the electrical-conductivity measurements. N.D.-G., N.K.-S., S.M., S.E.D. and R.P.D. contributed to performing a.c. magnetic-susceptibility measurements and analysed the data. N.D.-G., R.M. and R.P.D. contributed to performing heat-capacity measurements and the analysis. E.S., N.D.-G., R.M., D.D., H.P. and S.E.D. contributed to performing elemental analysis, EDX studies and XRD measurements. H.P., R.M., S.E.D. and R.P.D. contributed to performing Raman studies and H.P. and R.P.D. analysed the data. S.E.D. and A.S. performed structure analysis. H.P., S.E.D. and R.P.D. performed the magnetization measurements using a PPMS and R.P.D. analysed the data. K.V.L. and A.S. performed the simulations and analysed the data and chemistry protocol. N.D.-G., K.V.L., A.S., S.E.D. and R.P.D. wrote the paper. All authors discussed the results and commented on the manuscript. R.P.D. conceived the project and oversaw the entire project.

Competing interests The University of Rochester (U of R) has patents pending related to the discoveries of R.P.D. in the field of superconductivity. R.P.D. is a cofounder and chairman of the board of Unearthly Materials Inc. (UM), a Delaware corporation. UM has licensing agreements with U of R related to the patents, proprietary interests and commercialization rights related to the scientific discoveries of R.P.D. UM, U of R and R.P.D. are subject to non-disclosure and confidentiality agreements. A.S. is a cofounder, president, chief executive officer and board member of UM.

Additional information

Supplementary information The online version contains supplementary material available at https://doi.org/10.1038/s41586-023-05742-0.

Correspondence and requests for materials should be addressed to Ranga P. Dias.

Peer review information *Nature* thanks the anonymous reviewers for their contribution to the peer review of this work.

Reprints and permissions information is available at http://www.nature.com/reprints.

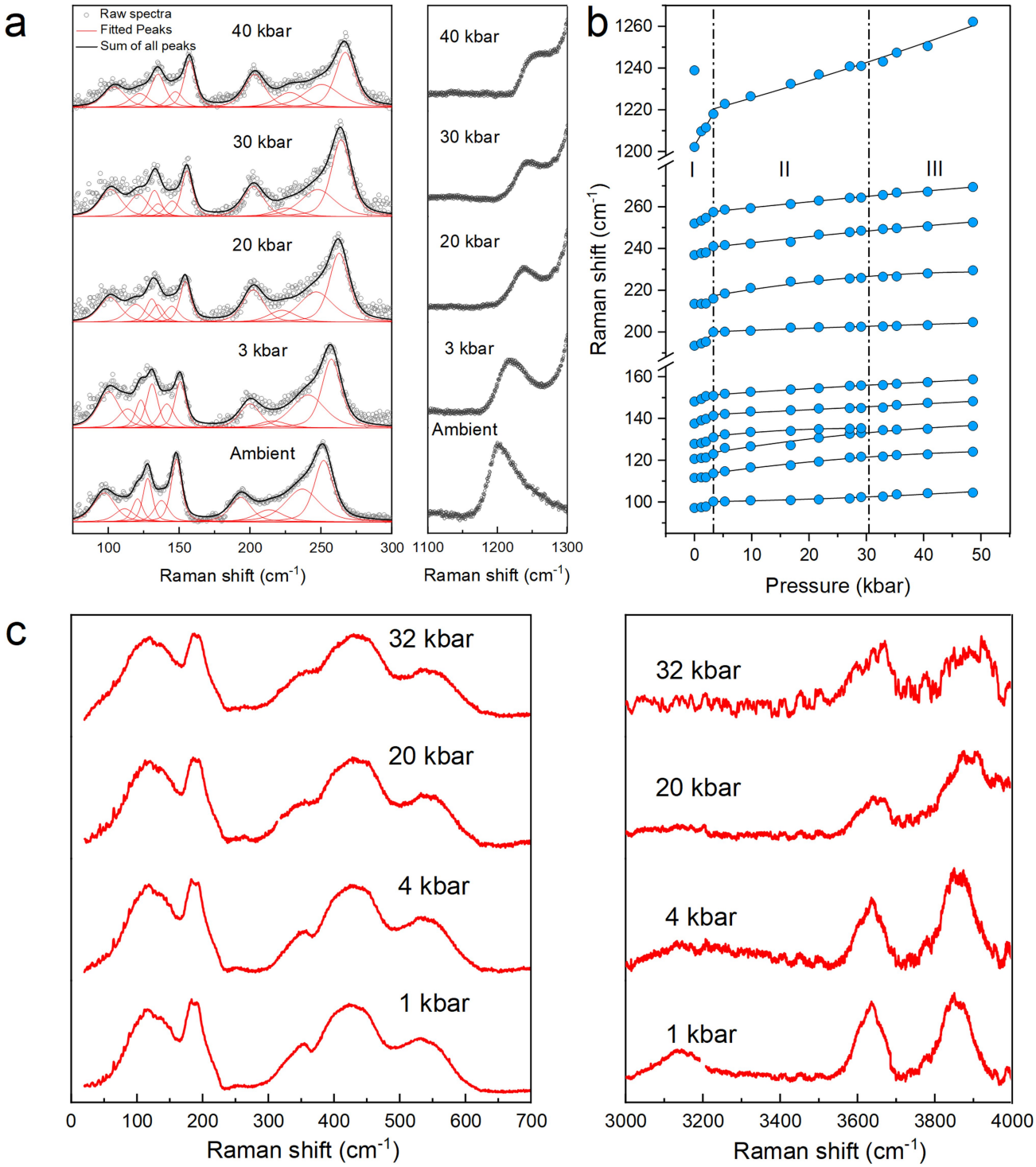

Extended Data Fig. 1 | Raman spectra. a, The spectral deconvolution of Raman spectra of compound A on compression. **b**, The Raman shift versus pressure of compound A at high pressures, indicating the three distinct phases. **c**, The spectral deconvolution of Raman spectra of compound B on compression.

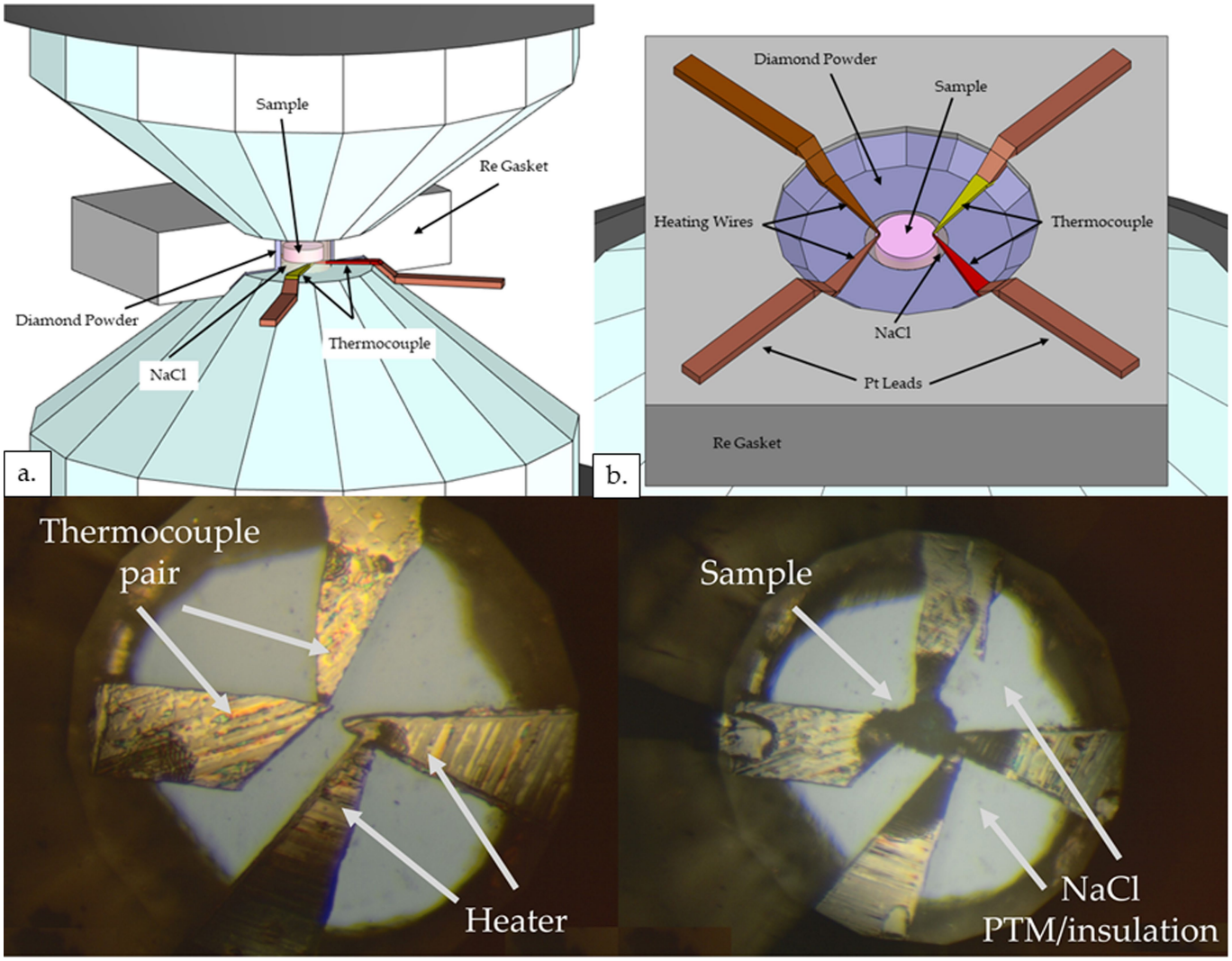

Extended Data Fig. 2 | The heat-capacity setup. Top, schematic rendering of the new a.c calorimetry technique (not to scale). The sample is surrounded by a NaCl insert with a heater and thermocouple making contact with the sample. **a**, View of the preparation as seen from the side showing the thermocouple making contact with the sample inside the DAC. **b**, View of the preparation as seen from the top of the sample area showing the configuration of heater, thermocouple and Pt leads. Bottom left, heat-capacity setup before loading sample. The thermocouple consists of a shorted alumel/chromel pair. The heater pair consists of a shorted metal, nichrome, Ti or Pt. When driven at frequency f, the sample temperature modulates at frequency $2 \times f$, which manifests as a voltage on the thermocouple pair that can be measured by a lock-in amplifier. Bottom right, after the sample is loaded, in contact with both the heater and the thermocouple, a small piece of NaCl is placed on top to thermally insulate it from the diamond.

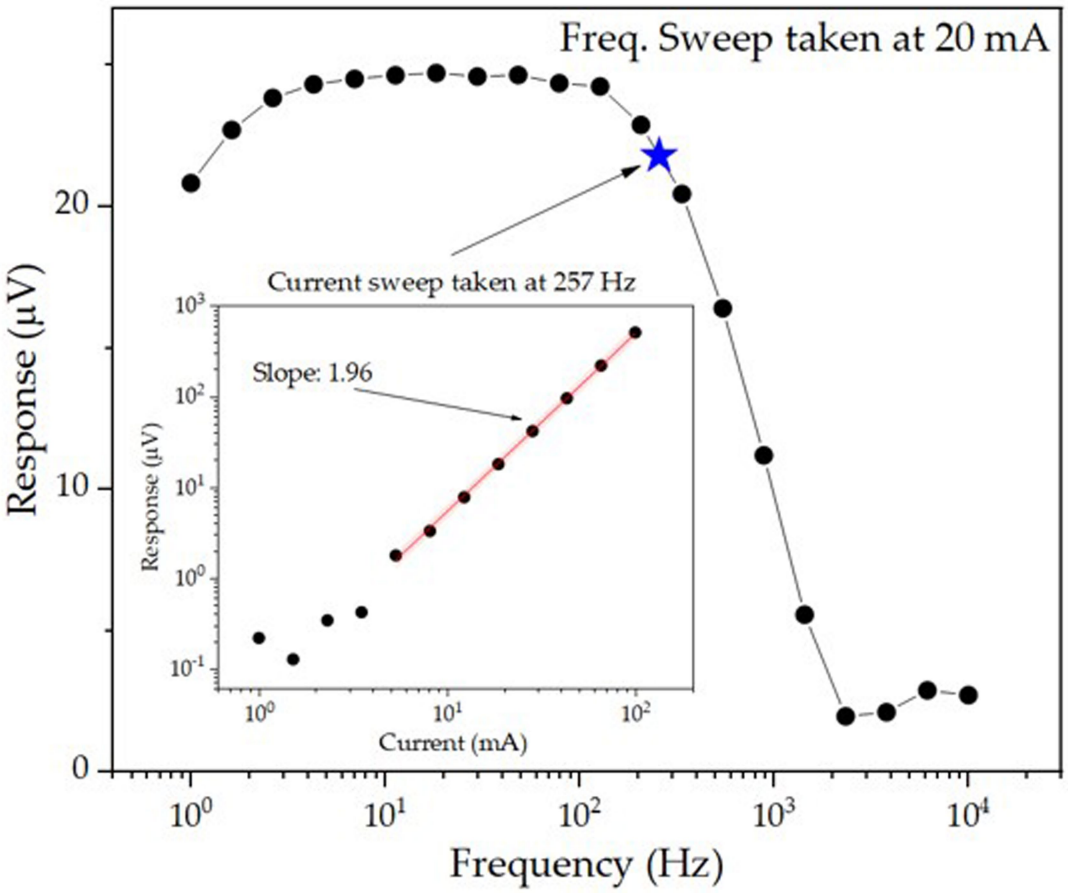

Extended Data Fig. 3 | Frequency response. Frequency and current sweeps measured on a heat-capacity setup before running the experiment. The frequency sweep shows the characteristic plateau and the current sweep demonstrates quadratic dependence, as expected from ohmic heating.

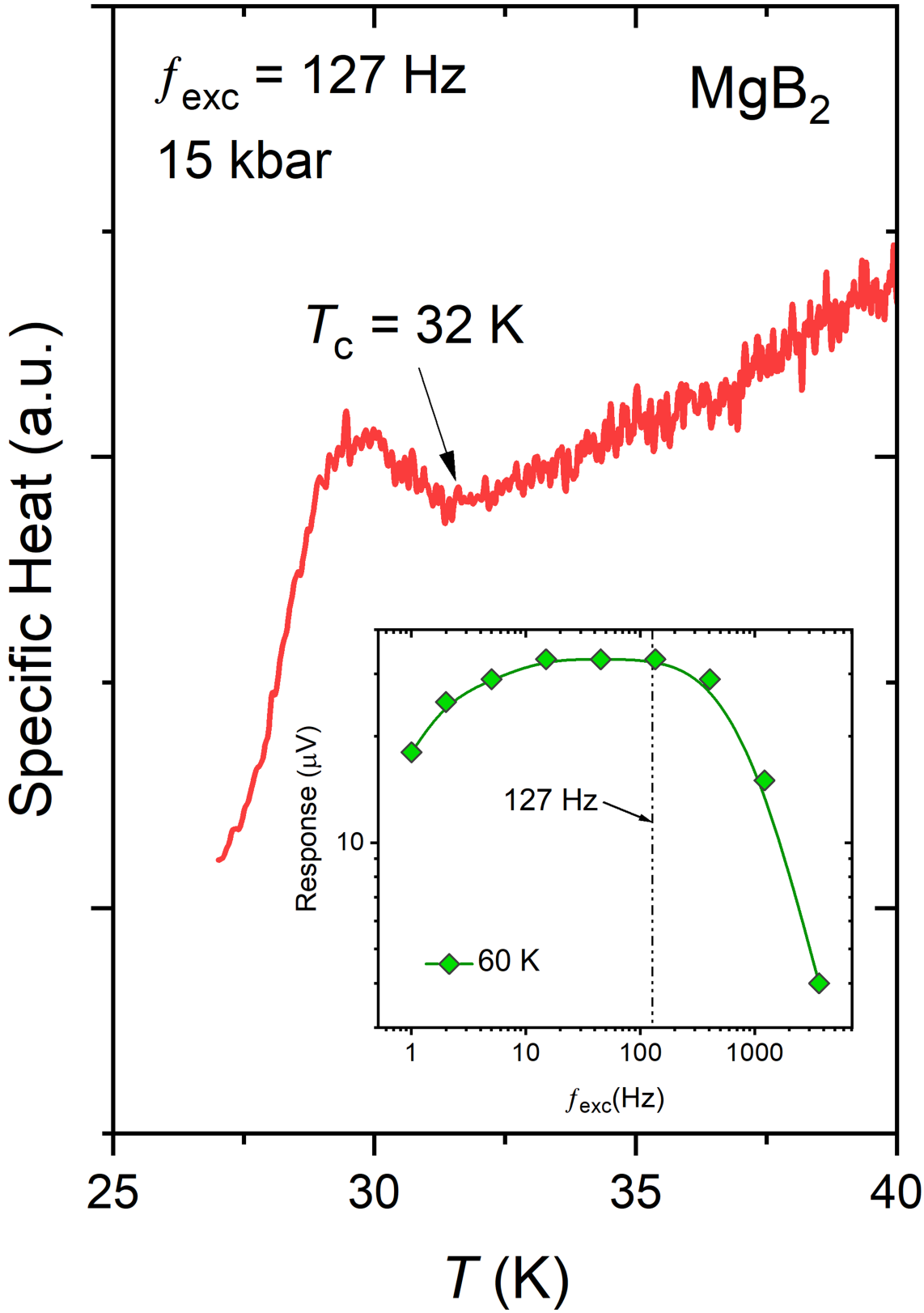

Extended Data Fig. 4 | Heat capacity. Specific heat capacity of MgB_2 as a function of temperature at 15 kbar and 127 Hz. The superconducting signature is clearly observed at 32 K. Inset, recorded lock-in voltages during the frequency sweeps at 60 K.

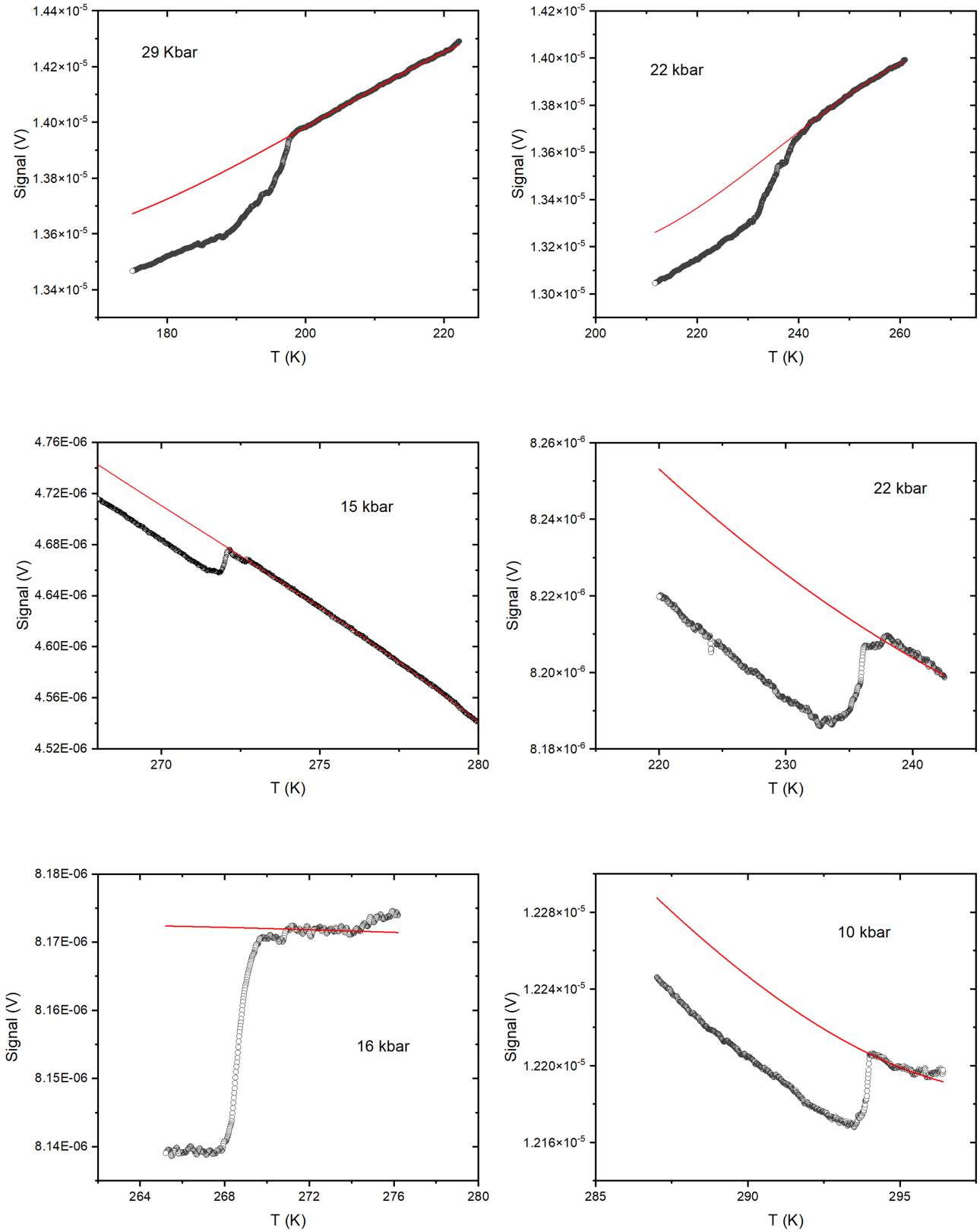

Extended Data Fig. 5 | a.c. susceptibility data before background subtraction. Voltage in volts versus temperature plots at different pressures before the background subtraction. Cubic or quadratic polynomial background was used for background subtraction for susceptibility data. This figure shows fittings with cubic or quadratic polynomials indicated by the red lines. For a.c. susceptibility data, the background subtraction was done mainly for visualization purposes.

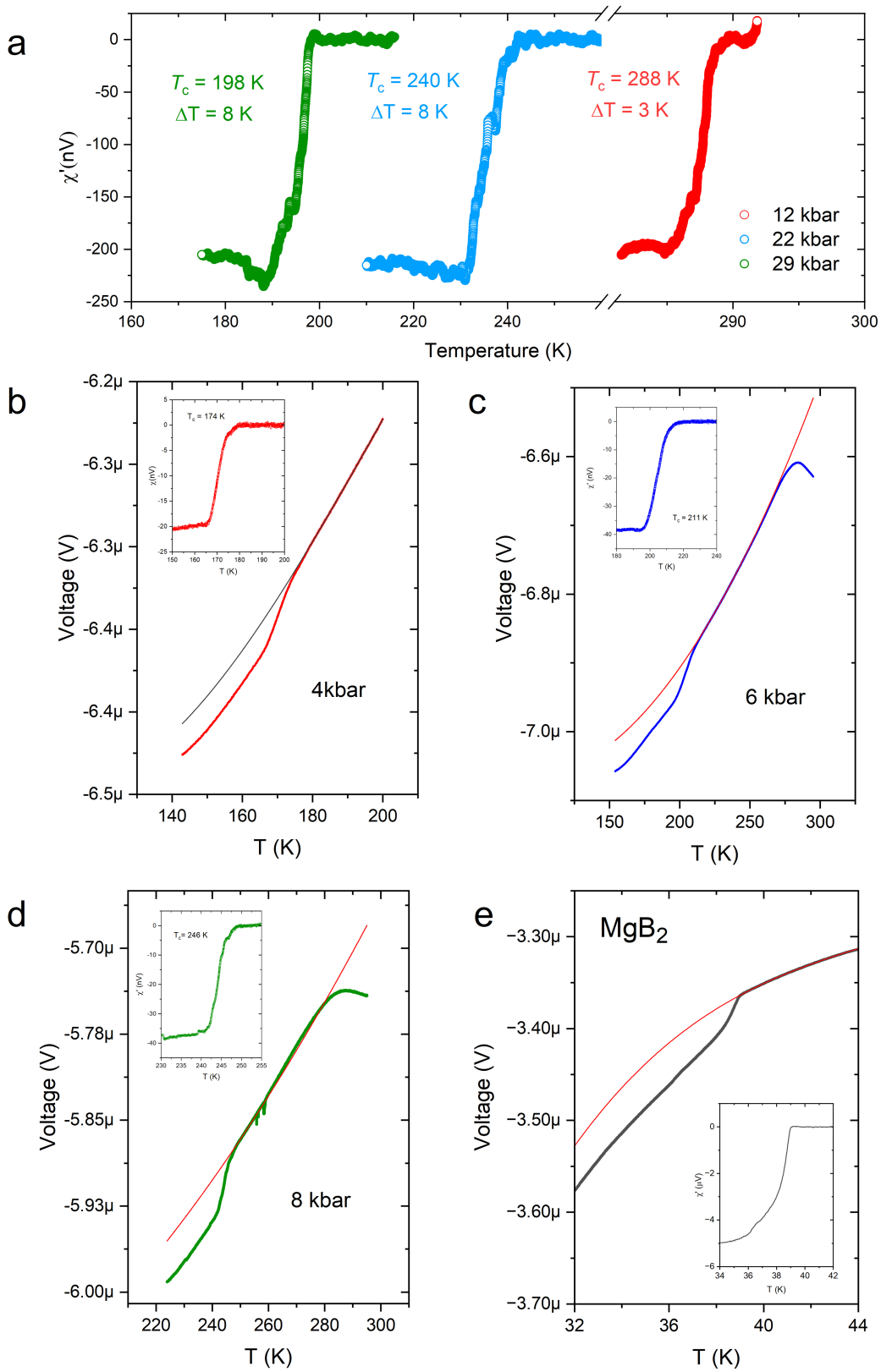

Extended Data Fig. 6 | Further a.c. susceptibility measurements. a, The a.c. susceptibility in nanovolts versus temperature for a larger sample of the N-doped Lu hydride system at select pressures from run 2, showing large diamagnetic signal of the superconducting transition owing to the large volume of the sample. The superconducting transition shifts rapidly under pressure to lower temperatures. a.c. susceptibility measurements taken over broader temperature ranges for N-doped Lu hydride at 4 kbar (**b**), 6 kbar (**c**) and 8 kbar (**d**). The red line in **b**–**d** is the quadratic fit for the background and the insets show the signals with the background subtracted. **e**, a.c. susceptibility measurements of MgB_2 as a function of temperature using exact same coil set up as the test sample.

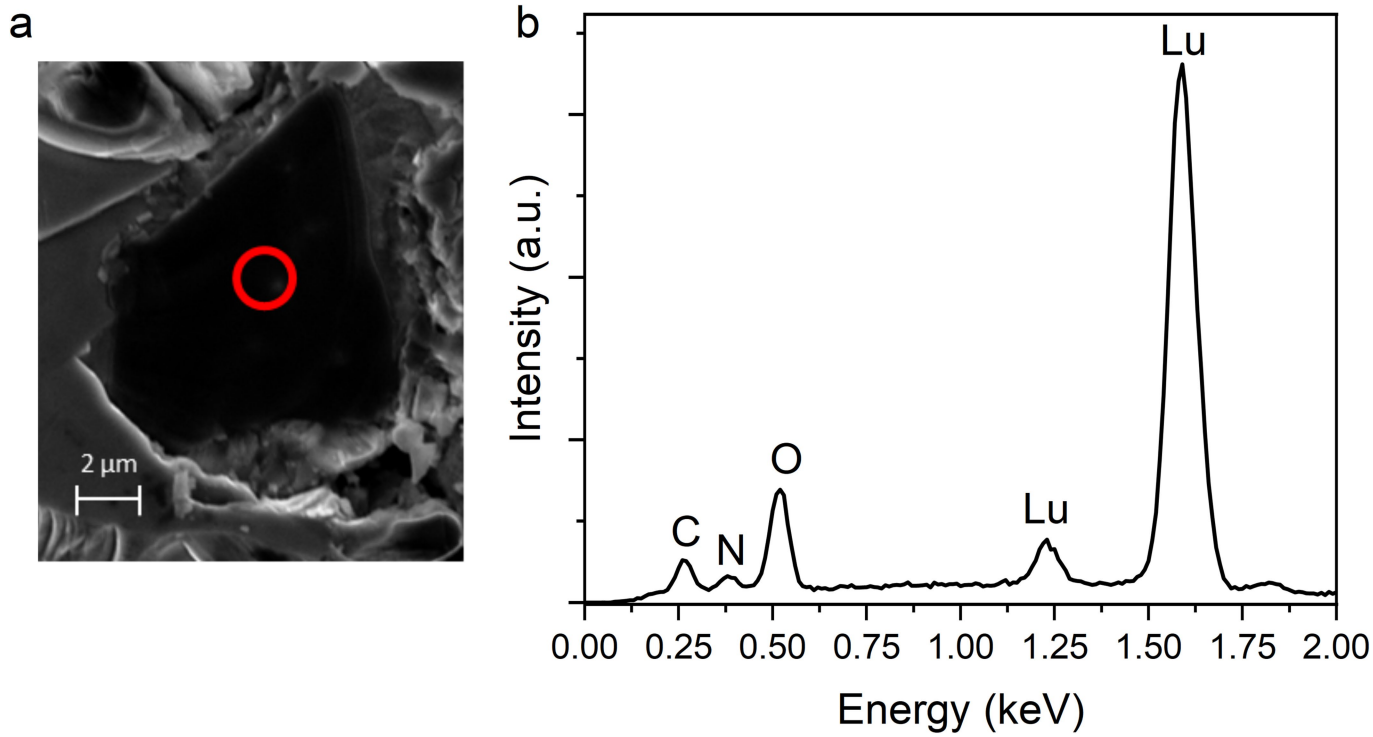

Extended Data Fig. 7 | EDX measurements. For EDX measurements, samples were prepared by mounting on an aluminium pin mount with double-sided carbon tape. The samples were then imaged using a Zeiss Auriga scanning electron microscope. Regions of interest were chosen by comparing the scanning electron microscopy image to a white-light image taken beforehand. EDX measurements were performed in the Zeiss Auriga scanning electron microscope with a driving energy of 15 kV and collected and analysed using an EDAX detector with the EDAX APEX software. Carbon and aluminium peaks seen in the EDX spectra originating from the carbon tape and aluminium mount required to place the samples into the scanning electron microscope vacuum chamber. EDX measurements provide further evidence for the presence of nitrogen in our samples.

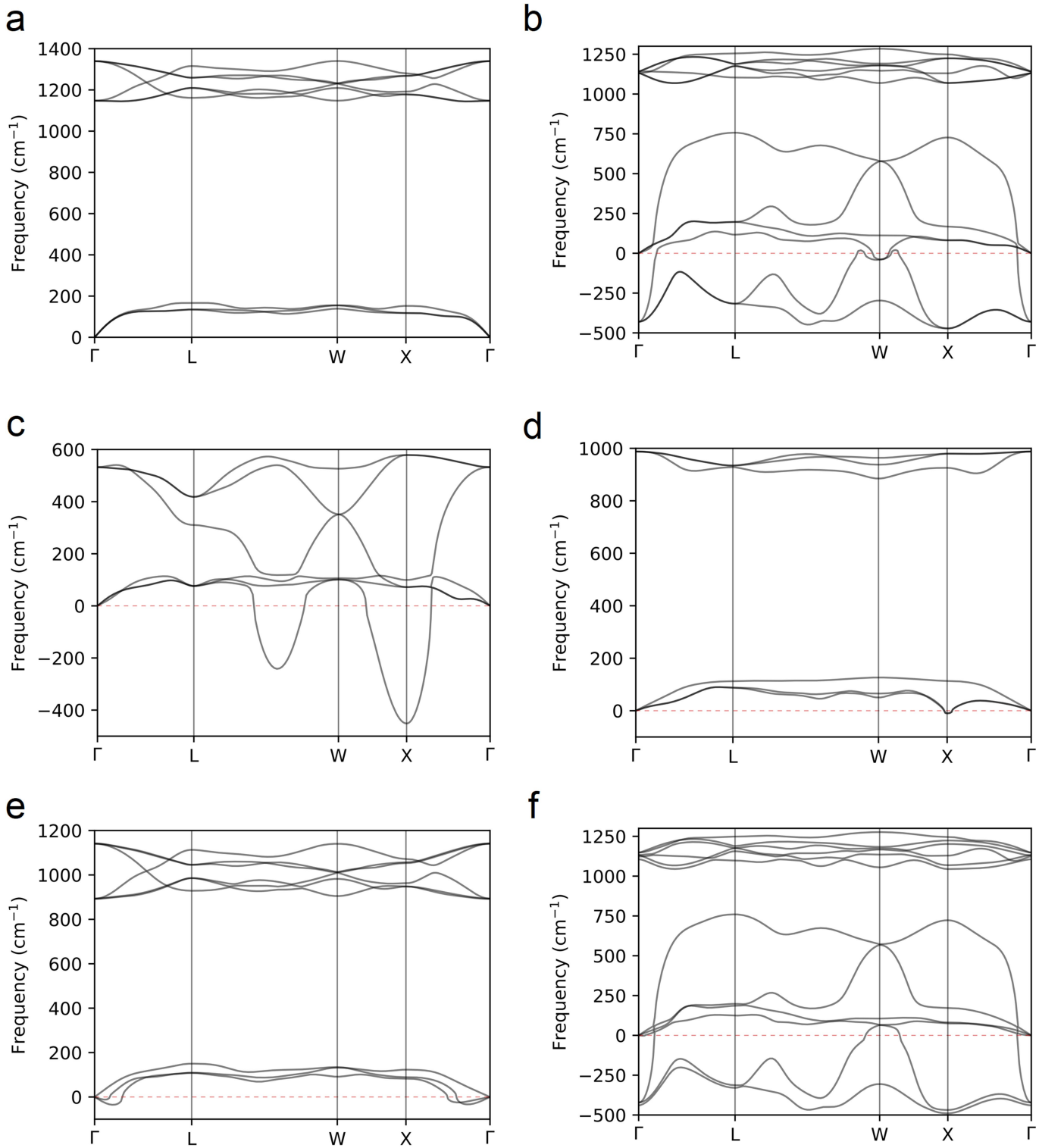

Extended Data Fig. 8 | Phonon bands of stoichiometric Lu hydrides. The calculated phonon band structures of 0 kbar LuH_2 in the fluorite structure (**a**), $Fm\overline{3}m$ LuH_3 (**b**), LuH in the RS structure (**c**) and LuH in the ZB structure (**d**). **e**, The calculated phonon band structures of 0 kbar LuH_2 in the fluorite structure using a triclinic representation of the lattice vectors with x parallel to a and z parallel to c^*, as opposed to the more highly symmetric lattice vectors for a primitive cell of a fcc cell; in this representation, the structure is represented with D_{3d} point-group symmetry as opposed to O_h point-group symmetry as in **a**. **f**, The calculated phonon band structures of 0 kbar LuH_3 using the same triclinic representation of the lattice vectors and point-group symmetry as in **e**.

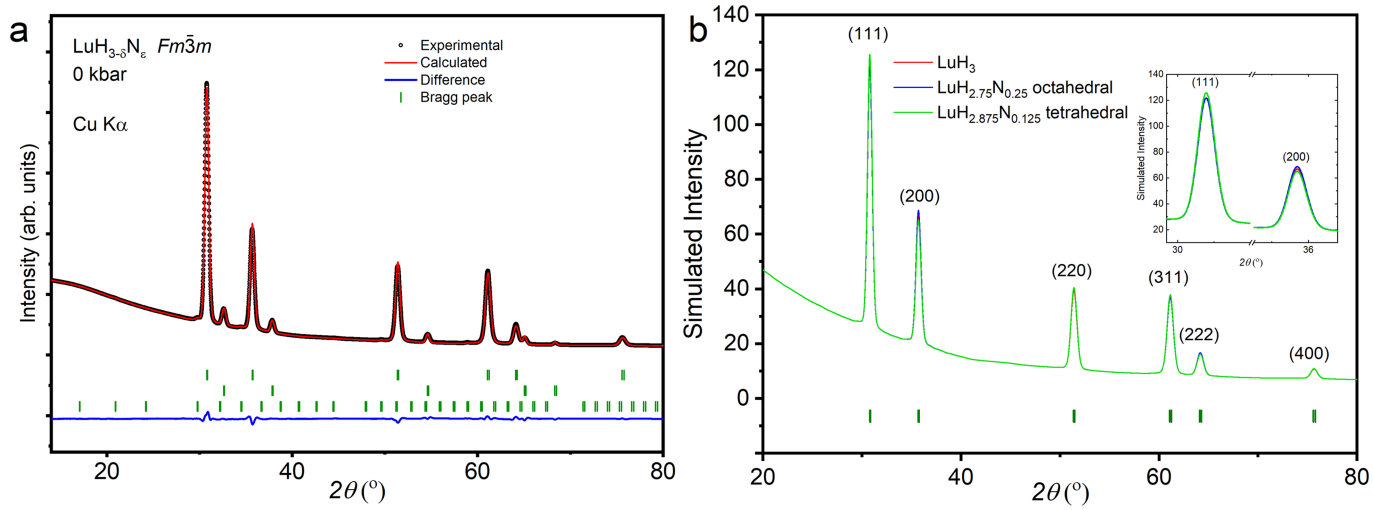

Extended Data Fig. 9 | Rietveld refinement of site occupancies. a, Rietveld refinement of the X-ray powder diffraction data collected at 295 K with Cu Kα radiation with refining the occupancy of the tetrahedral interstitial site with N for nitrogen-doped lutetium hydride. **b**, Simulation of the XRD pattern with Cu Kα wavelength for LuH_3 (red), LuH_3 with a N replacing a single H in an octahedral site (blue) and a tetrahedral site (green). Rietveld refinement of the X-ray powder diffraction data of ground powder sample was performed with an attempt to investigate the possible N substitution in nitrogen-doped lutetium hydride. We note here that XRD is mostly dominated by heavy Lu atoms.

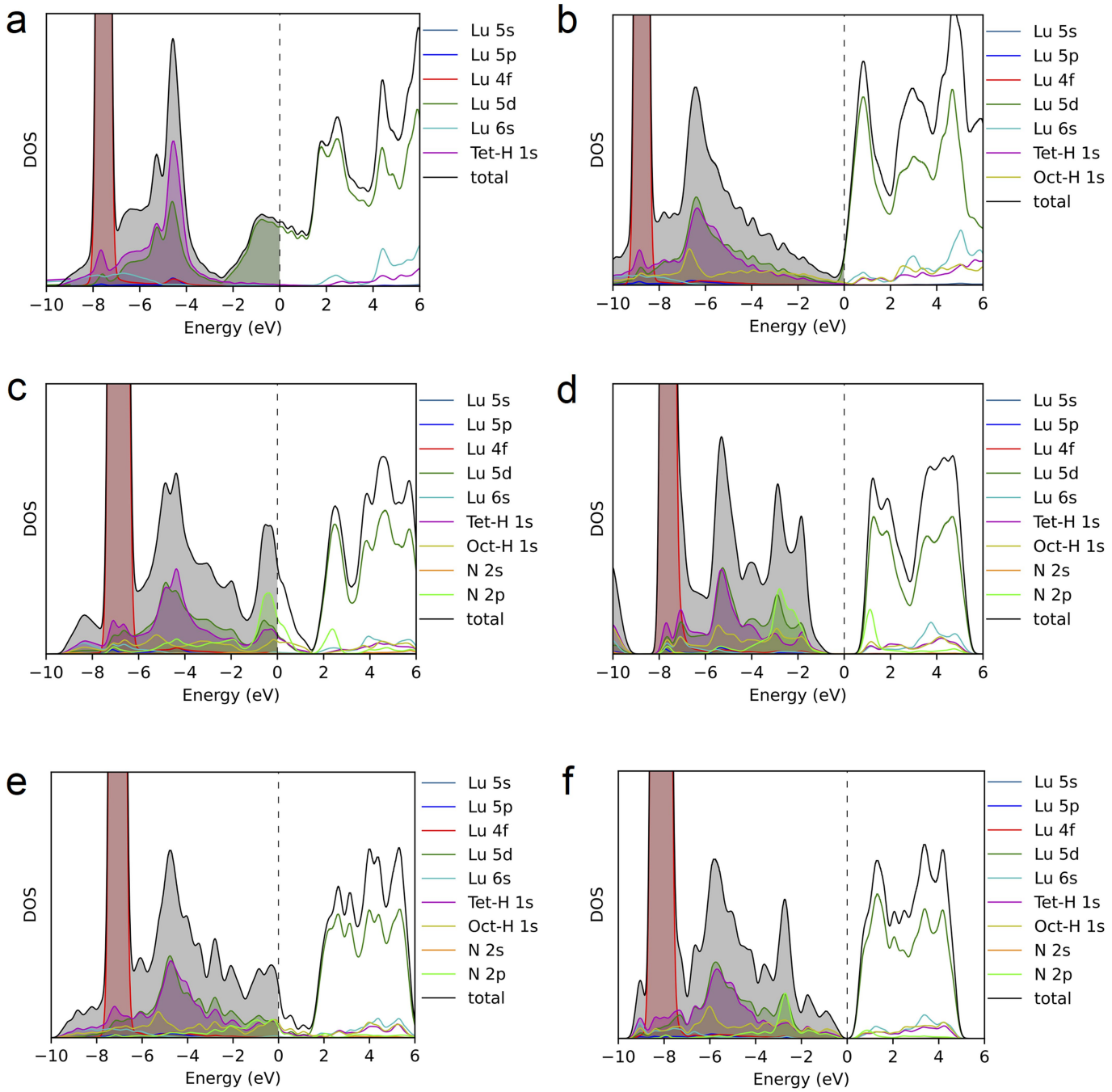

Extended Data Fig. 10 | Projected density of states. The atom and angular momentum projected partial density of states of LuH_2 in the fluorite structure (**a**); $Fm\bar{3}m$ LuH_3 (**b**); the cubic cell of $Fm\bar{3}m$ LuH_3 with a N substituted for a H in an octahedral (**c**) and tetrahedral (**d**) interstice; and a 2 × 2 × 2 supercell of the rhombohedral primitive cell of $Fm\bar{3}m$ LuH_3 with a N substituted for a H in an octahedral (**e**) and tetrahedral (**f**) interstice. In the legends, Oct- means hydrogens in the octahedral interstices and Tet- means hydrogens in the tetrahedral interstices. Each channel is summed over all similar atoms in the unit cell and the plots are scaled to represent a maximum value of 2.5 states eV^{-1} per formula unit.

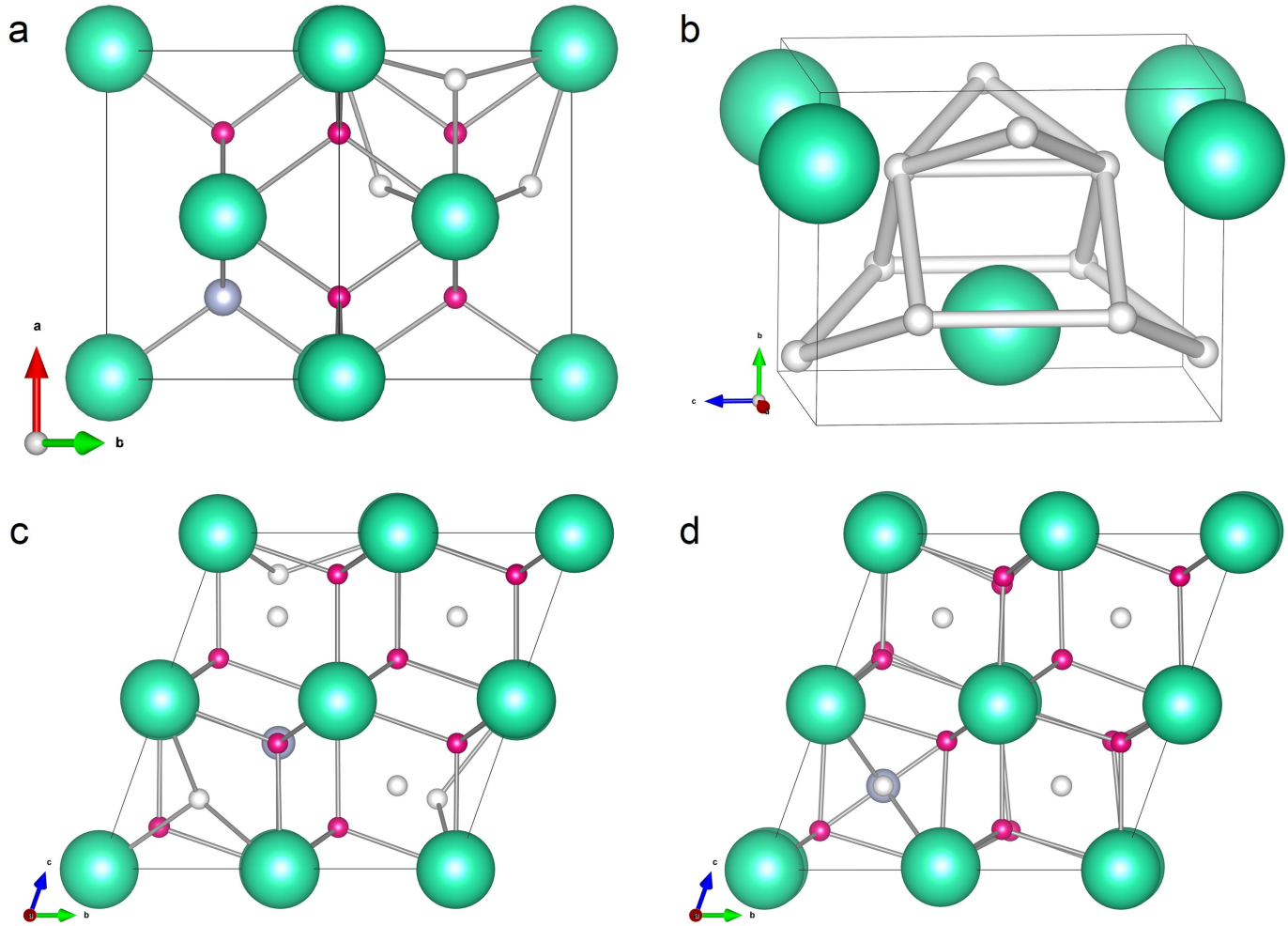

Extended Data Fig. 11 | Distorted structures predicted by DFT. a, The distortions to the octahedral hydrogens observed by substituting a N atom for a tetrahedral atom in a single unit cell of $Fm\bar{3}m$ LuH_3. **b**, The *Pmnm* LuH_3 structure found by perturbing the cubic $Fm\bar{3}m$ unit cell of LuH_3, which suggests possible light-atom positions in phase III. **c**, The lattice distortions from substituting a N into a tetrahedral interstice in a 2 × 2 × 2 supercell of the rhombohedral primitive of LuH_3. **d**, The lattice distortions from substituting a N into an octahedral interstice in a 2 × 2 × 2 supercell of the rhombohedral primitive of LuH_3. The lutetium atoms are green, the nitrogen atoms are lavender and the hydrogen atoms in octahedral interstitial sites are white and those in tetrahedral interstitial sites are pink. In **b**, there is no distinction made between the hydrogen atom sites, so they are all white.

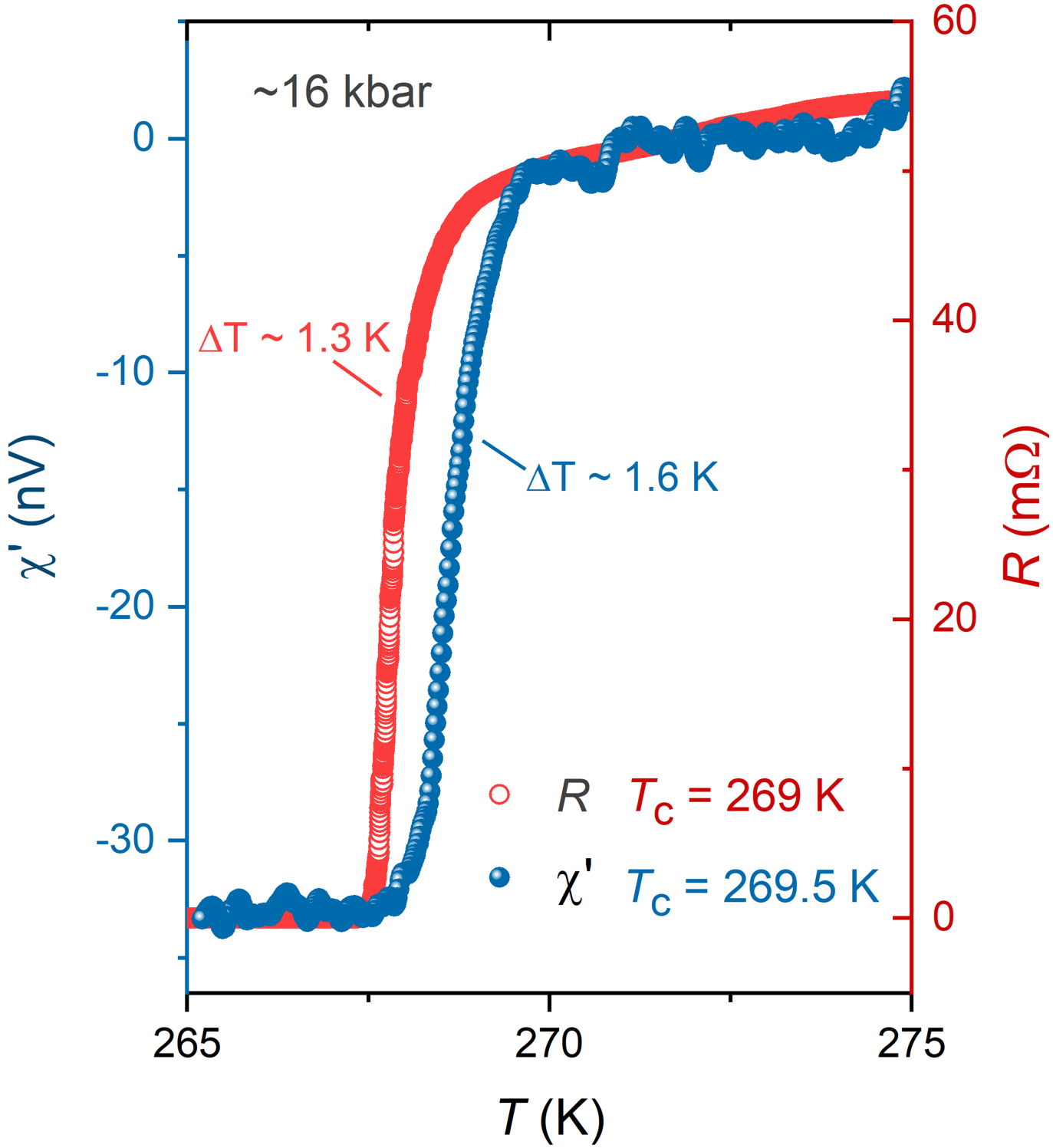

Extended Data Fig. 12 | Superconducting transition widths. For comparison, the superconducting transition obtained from electrical measurements and a.c. susceptibility measurement at a similar pressure (16 kbar) is shown by red and blue, respectively. The transition width of the resistance drop is 1.3 K and 1.6 K for the a.c. magnetic susceptibility measurement.

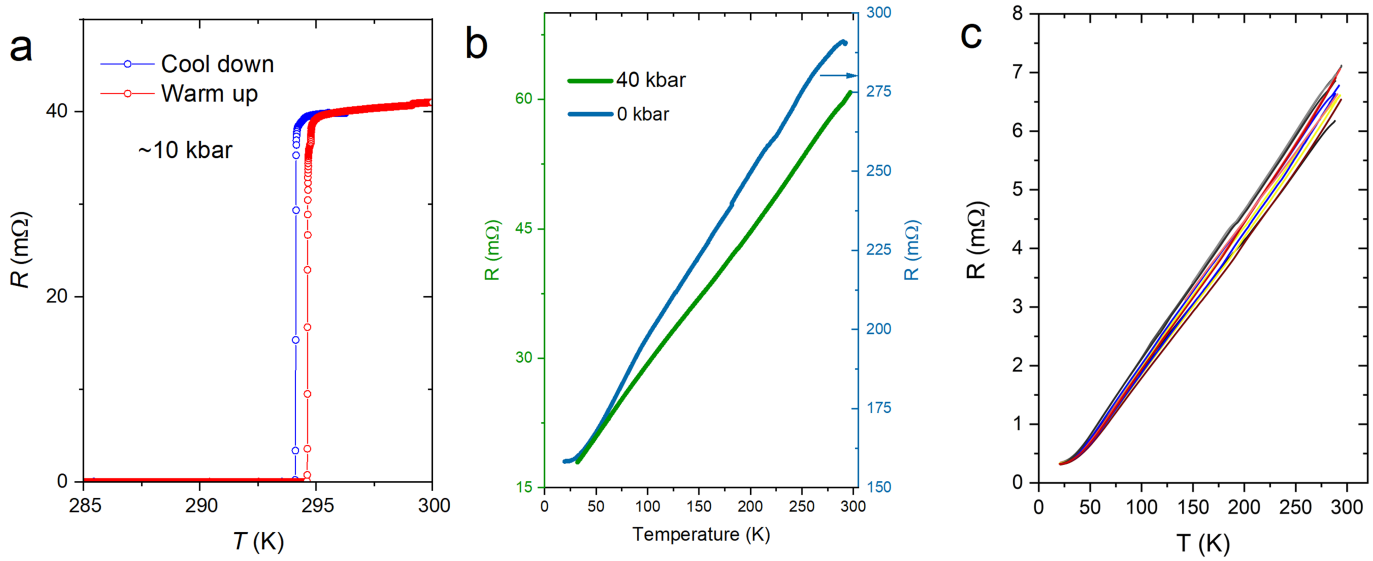

Extended Data Fig. 13 | Low-temperature electrical-resistance behaviour of N-doped Lu–H systems. a, The resistance measured on both warming and cooling at about 10 kbar. **b**, Temperature-dependent electrical resistance of phases I and III, showing the non-superconducting state. **c**, Four-probe electrical-resistance measurements of different Lu–H–N samples, which consistently shows highly metallic behaviour with decreasing temperature.

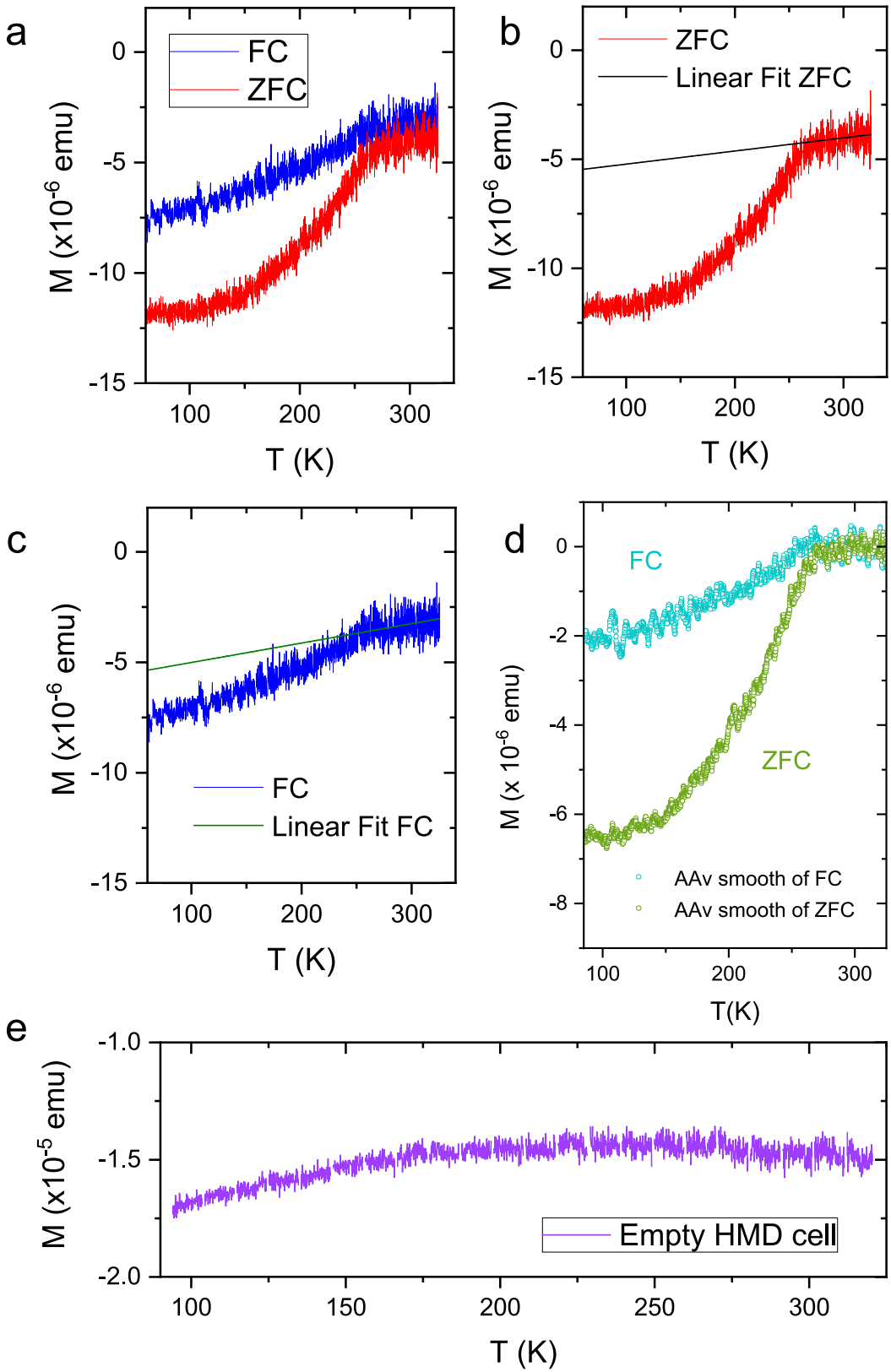

Extended Data Fig. 14 | Magnetic-susceptibility background and smoothing. a–**c**, The ZFC and FC magnetization versus temperature at 8 kbar used to construct Fig. 3a, along with a linear fit to the data at temperatures above the transition temperature, which was used for the background subtraction. **d**, The ZFC and FC curves with the linear backgrounds shown in **b** and **c** subtracted out, as well as with a ten-point adjacent-average smoothing applied. **e**, The measured cell background at 60 Oe for the HMD cell used for the d.c. measurements.

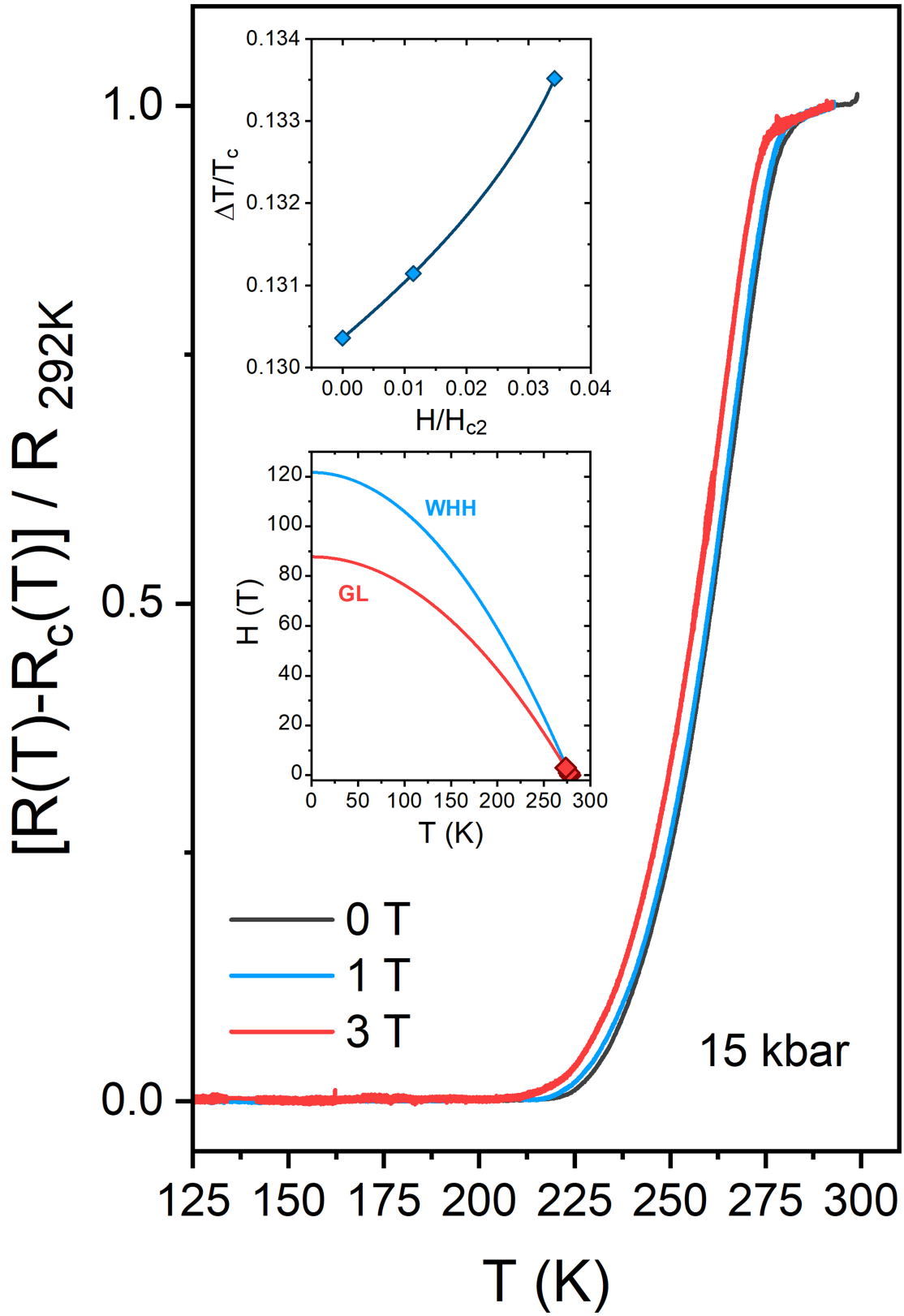

Extended Data Fig. 15 | See next page for caption.

Extended Data Fig. 15 | Electrical-resistance behaviour under magnetic field. Low-temperature electrical-resistance behaviour under magnetic fields of $H = 0$ T, 1 T and 3 T (increasing from right to left) at 15 kbar. In this study, the superconductivity of nitrogen-doped lutetium hydride is suppressed by the application of a 3-T external magnetic field, reducing T_c by about 5 K at 15 kbar, further confirming a superconducting transition. The temperature dependence of the resistance of a simple metal is written as: $R(T) = R_0 + aT^2 + bT^5$. We fit the data below $T < 220$ K for each field, at which the resistance goes to the minimum value, to that function and subtracted it out. Inset top, the superconducting transition width, ΔT_c, at 15 kbar slightly increases under external magnetic fields. The ΔT_c has a good linear relationship with the applied magnetic field, as expected from the percolation model. The superconducting transition width is defined here as $\Delta T_c = T_{90\%} - T_{10\%}$, in which $T_{90\%}$ and $T_{10\%}$ are the temperatures corresponding to 90% and 10% of the resistance at 292 K, respectively. Fitting to the linear relation of $\Delta T_c = \Delta T_c(0) + kH_{c2}$, in which $\Delta T_c(0)$ is the width at zero external field and k is a constant, provides the values $\Delta T_c(0) = 36.3$ K and $k = 0.07$ K T^{-1}. The large transition width at zero field indicates sample inhomogeneities, which is typical for high-pressure experiments. Inset bottom, the temperature dependence of the upper critical field, $H_c(T) = H_c(0)\left[1 - \left(\frac{T}{T_c}\right)^2\right]$, can be expressed using GL theory or the conventional Werthamer–Helfand–Hohenberg model. The GL model in the limit of zero temperature yields $H_{c2}(0) \approx 88$ T. From the Werthamer–Helfand–Hohenberg model in the dirty limit, $H_{c2}(0)$ can be extrapolated from the slope of the H–T curve as $H_{c2}(0) = 0.693 \left|\frac{dH_{c2}}{dT}\right|_{T=T_c} T_c$, which yields roughly 122 T.

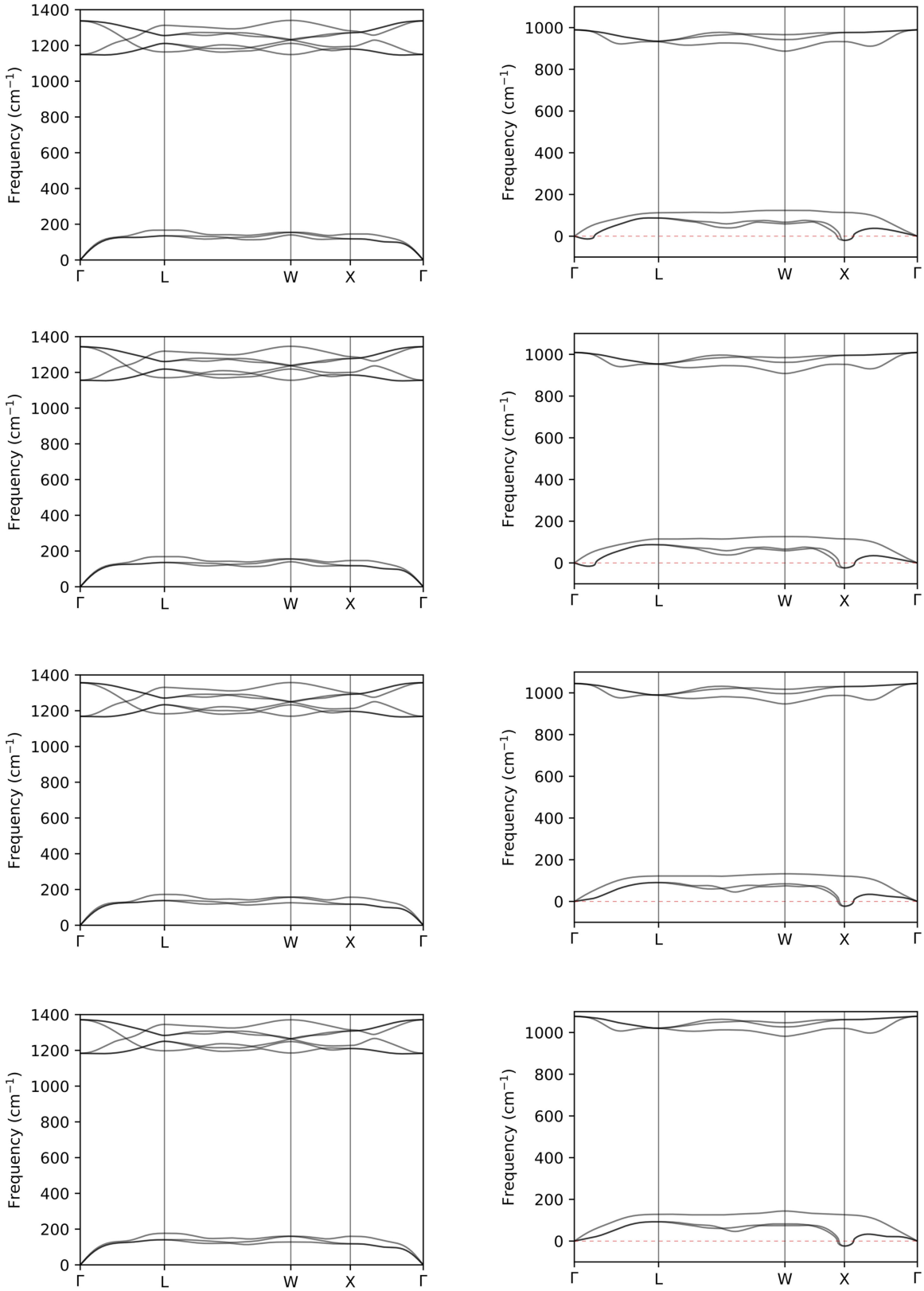

Extended Data Fig. 16 | Phonon bands of pressurized stoichiometric Lu hydrides. The calculated phonon band structures of LuH_2 in the fluorite structure (left) and LuH in the ZB structure (right) at 0 kbar (top row), 10 kbar (second row), 30 kbar (third row) and 50 kbar (bottom row). The electronic smearing width is 0.005 Ry and the lattice vectors are the highly symmetric ones for a fcc cell. Negligible change in the computed electron–phonon couplings or logarithmic frequency is seen for LuH_2 on pressurization.